



**HAL**  
open science

## The Jo-In protein welding system is a relevant tool to create CBM-containing plant cell wall degrading enzymes

Louise Badruna, Vincent Burlat, Pierre Roblin, Thomas Enjalbert, Guy Lippens, Immacolata Venditto, Michael O'donohue, Cédric Montanier

### ► To cite this version:

Louise Badruna, Vincent Burlat, Pierre Roblin, Thomas Enjalbert, Guy Lippens, et al.. The Jo-In protein welding system is a relevant tool to create CBM-containing plant cell wall degrading enzymes. *New Biotechnology*, 2021, 65, pp.31-41. 10.1016/j.nbt.2021.07.004 . hal-03340154

**HAL Id: hal-03340154**

**<https://hal.inrae.fr/hal-03340154v1>**

Submitted on 2 Jun 2023

**HAL** is a multi-disciplinary open access archive for the deposit and dissemination of scientific research documents, whether they are published or not. The documents may come from teaching and research institutions in France or abroad, or from public or private research centers.

L'archive ouverte pluridisciplinaire **HAL**, est destinée au dépôt et à la diffusion de documents scientifiques de niveau recherche, publiés ou non, émanant des établissements d'enseignement et de recherche français ou étrangers, des laboratoires publics ou privés.



17 Abstract:

18 Irrespective of their biological origin, most proteins are composed of several  
19 elementary domains connected by linkers. These domains are either functionally independent  
20 units, or part of larger multidomain structures whose functions are defined by their spatial  
21 proximity. Carbohydrate-degrading enzymes provide examples of a range of multidomain  
22 structures, in which catalytic protein domains are frequently appended to one or more non-  
23 catalytic carbohydrate-binding modules which specifically bind to carbohydrate motifs. While  
24 the carbohydrate-binding specificity of these modules is clear, their function is not fully  
25 elucidated. Herein, an original approach to tackle the study of carbohydrate-binding modules  
26 using the Jo-In biomolecular welding protein pair is presented. To provide a proof of concept,  
27 recombinant xylanases appended to two different carbohydrate-binding modules have been  
28 created and produced. The data reveal the biochemical properties of four xylanase variants  
29 and provide the basis for correlating enzyme activity to structural properties and to the nature  
30 of the substrate and the ligand specificity of the appended carbohydrate-binding module. It  
31 reveals that specific spatial arrangements favour activity on soluble polymeric substrates and  
32 that activity on such substrates does not predict the behaviour of multimodular enzymes on  
33 insoluble plant cell wall samples. The results highlight that the Jo-In protein welding system  
34 is extremely useful to design multimodular enzyme systems, especially to create rigid  
35 conformations that decrease the risk of intermodular interference. Further work on Jo-In will  
36 target the introduction of varying degrees of flexibility, providing the means to study this  
37 property and the way it may influence multimodular enzyme functions.

38

39 Keywords:

40 GH family 11 endo-1,4- $\beta$ -xylanase, CBM family 2, CBM family 3, Bio Molecular Welding,  
41 spatial proximity

42

43 Abbreviations

44 GH – glycoside hydrolase; CBM – carbohydrate-binding module; PCW – plant cell wall;  
45 SAXS - Small angle X-ray scattering; MST - Microscale Thermophoresis; ITC - Isothermal  
46 titration calorimetry; NMR - Nuclear Magnetic Resonance; RC - regenerated cellulose; CN -  
47 cellulose nanocrystals.

48

## 49 **Introduction**

50 Domains constitute the key building blocks of proteins, conferring their structural  
51 integrity and/or functionalities. They can form independent structural and or functional units,  
52 but are often combined in multidomain organizations in which neighboring domains associate  
53 to define protein structures and/or functions [1]. The majority of proteins from all taxa are  
54 composed of several domains connected by linkers [2,3]. This quite complex organization is  
55 probably the source of functional diversity and also responsible for functional fine-tuning [4],  
56 including that of enzymes whose catalytic sites are often formed at the interface of several  
57 domains [5].

58 Plant cell wall-degrading enzymes provide excellent examples of multidomain proteins.  
59 This large group is characterized by a multitude of structures and functions, their diversity  
60 matching the complexity of plant cell wall (PCW) structures [6]. Lignified PCWs are  
61 macromolecular networks, composed of cellulose, hemicelluloses, pectins, proteins and  
62 lignins that interact and, in some cases, crosslink to form insoluble, three dimensional  
63 matrices [7]. The main enzymes involved in the breakdown of PCWs are glycoside  
64 hydrolases (GHs), a large and diverse group including cellulases, hemicellulases and  
65 pectinases. Most GHs display modular architecture, containing catalytic and non-catalytic  
66 domains [8,9]. Regarding the latter, carbohydrate binding modules (CBMs) are prominent.

67 When appended to a catalytic module, CBMs target specific regions in polysaccharides,  
68 consequently increasing the local concentration of catalytic domains and favoring intimate  
69 contacts between the substrate and the enzyme. In certain cases, CBMs also disrupt the  
70 surface of tightly packed polymers, such as cellulose or starch, thus facilitating enzyme action  
71 [10].

72

73 In PCW-degrading enzymes, domain organizations are numerous and quite varied. In  
74 some cases, the catalytic GH domain and the CBM are combined in a single prolonged  
75 domain, while in others the CBM is appended to the GH *via* a linker peptide of variable size  
76 (from 4 to 158 residues), composition and structure [11]. Considering the number of known  
77 GH and CBM domains and the number of possible combinations, the organizational diversity  
78 of PCW-degrading enzymes is considerable [12].

79

80 Previous studies described the creation of synthetic multimodular GH constructs [13–15]  
81 designed to investigate enzymatic activity. Often, a domain fusion strategy was adopted,  
82 using short linker sequences to associate different domains in recombinant proteins. While  
83 this strategy is frequently employed, its success hinges on expression of the fusion protein and  
84 requires the cloning and expression of each studied domain combinations. An alternative  
85 route to obtain a range of different domain combinations is to express single domains  
86 separately and then perform module linkage in a second *in vitro* step. Several strategies to  
87 achieve this have also been described [16–21]. One of the more recent additions to the protein  
88 engineer's toolbox is genetically encoded click chemistry (GECC), based on a naturally  
89 occurring phenomenon identified in bacterial pili, where certain protein subunits are linked  
90 together *via* an isopeptide bond [22]. Exploiting this for protein engineering has led to the  
91 development of SpyTag-SpyCatcher [23] and the Biomolecular Welding tool [24]. The latter

92 comprises two proteins, designated Jo and In (10.6 and 16.5 kDa, respectively), which  
93 spontaneously form an intramolecular isopeptide bond when mixed in solution, leading to a  
94 two-domain protein measuring 6 nm in length. When Jo and In are individually fused to other  
95 protein domains, it is possible to create domain combinations *in vitro*, with the Jo-In  
96 intramolecular complex acting as the linker. Accordingly, Jo-In were recently used to  
97 combine two different GHs, producing bifunctional enzymes [25].

98

99 In the current study, focusing on the well characterized xylanase Xyn11A from  
100 *Neocallimastix patriciarum* [26] Jo-In is used to link this GH to two different, non-cognate  
101 CBMs of bacterial origin either targeting the substrate of Xyn11A (xylan) or another PCW  
102 polymer (cellulose), the aim being to understand how the specific properties of these CBMs  
103 affect enzyme activity on simple substrates and complex PCW networks.

104

## 105 **Materials and methods**

### 106 **Gene cloning**

107 Plasmid constructs used are summarized in Supplementary Table S1. For some cloning  
108 purposes, PCR (Phusion™ High-Fidelity DNA Polymerase, ThermoFischer Scientific,  
109 Waltham, MA, USA) was used to amplify target sequences, generally introducing restriction  
110 enzyme target sequences, and to introduce PCR amplicons into linearized plasmid vectors by  
111 homologous recombination (In-Fusion® HD cloning kit, Clontech, Mountain View, CA,  
112 USA). Alternatively, target sequences were synthesized by Genscript HK limited  
113 (Piscataway, NJ, USA) introducing appropriate restriction enzyme target sequences for  
114 subsequent plasmid construction.

115

### 116 **Protein expression and purification**

117 Proteins were expressed in *Escherichia coli* strain BL21 (DE3) or Tuner (DE3) harbouring  
118 the relevant plasmids and purified using standard methods described in Supplementary Table  
119 S2.

120

### 121 **Covalent chimeric protein complexes**

122 To prepare chimeric protein complexes, purified Jo and In fusion proteins were mixed, using  
123 a slightly lower concentration for the xylanase than for the CBMs (typically 2  $\mu$ moles of  
124 xylanase for 3  $\mu$ moles of CBM, 8.3 and 8.8 mg/ml of protein, respectively), for 1 h at 21°C  
125 and then stored overnight at 4 °C. Protein complexes were isolated from solution using a  
126 XK16 Hiload 16/600 Superdex S75 prep-grade gel filtration column (GE Healthcare Life  
127 Sciences, Chicago, IL, USA) connected to an Äkta Pure system. Elution was performed at 1  
128 mL/min using 50 mM sodium phosphate buffer pH 7.4 supplemented with 150 mM NaCl.  
129 Subsequently, NaCl was removed by dialysis and purified chimeric complexes were judged  
130 homogenous by sodium dodecyl polyacrylamide gel electrophoresis (SDS-PAGE).

131

### 132 **Enzymatic activity measurements**

133 The apparent kinetic parameters  $K_{Mapp}$ ,  $V_{max}$ ,  $k_{cat}$ , and  $k_{cat}/K_{M app}$  of Jo-NpXyn11A were  
134 measured using the dinitrosalicylic acid (DNSA) assay as previously described [25], using  
135 various concentrations (0.3 to 30 mg/mL) of beechwood xylan (BWX, Megazyme) in activity  
136 assay buffer (50 mM sodium phosphate, 12 mM sodium citrate pH 6, supplemented with 1  
137 mg/mL of bovine serum albumin (BSA, Merck KGaA, Darmstadt, Germany). DNSA assays  
138 were performed to determine the specific activity (SA) of xylanase derivatives (5 nM) on  
139 0.5% (w/v) wheat arabinoxylan (WAX), 0.5% (w/v) rye arabinoxylan (RAX) or 1% (w/v)  
140 BWX respectively (all from Megazyme, Bray, Ireland) in 50 mM Tris-HCl pH 7.5,  
141 supplemented with 1 mg/mL of BSA as previously described [27]. SA of the xylanases (100

142 nM) was also determined using 4-nitrophenyl- $\beta$ -D-xylotrioside (*p*NP-X<sub>3</sub>, LIBIOS, France)  
143 using 5 mM of substrate in activity assay buffer as previously described [25]. SA were  
144 expressed in  $\mu$ moles of product formed per min per  $\mu$ mole of enzyme (IU/ $\mu$ mole) in order to  
145 integrate the differences of mass concentration [25]. To investigate enzyme activity on  
146 complex substrates, 5 g destarched wheat bran and 10 g wheat straw (0.5 mm) (both from  
147 ARD, Pomacle, France), were each washed in 2 L of deionized water for 1 h at 4 °C and  
148 recovered by filtration (0.45  $\mu$ m) before drying at 50 °C for 3 d. For enzyme assays, wheat  
149 bran or straw (2 % w/v) were incubated overnight in 1.9 mL of activity assay buffer before  
150 the addition of enzyme (final concentration 1  $\mu$ M). Reactions were conducted at 37 °C under  
151 constant mixing at 1200 rpm (ThermoMixer<sup>®</sup> C, Eppendorf, Hamburg, Germany). Reaction  
152 progress was monitored by regular sampling as previously described [25]. All experiments  
153 were performed in triplicate, and the reported values are the means of three experiments  $\pm$  SD.  
154 Kinetic parameters were derived from the data using the Michaelis-Menten equation  
155 embedded in SigmaPlot 11.0 (Systat Software, San Jose, CA, USA).

156

### 157 **Isothermal titration calorimetry (ITC)**

158 ITC measurement was carried out using a MicroCal VP-ITC titration calorimeter (Malvern  
159 Panalytical, Malvern, UK) as detailed in Supporting Information. Integrated heat effects were  
160 analyzed by non-linear regression using a single-site binding model (Microcal ORIGIN  
161 software, version 7.0, Microcal Software), yielding values for the association constant  $K_a$  ( $M^{-1}$ )  
162 and the binding enthalpy  $\Delta H$  ( $J \cdot mol^{-1}$ ). Other thermodynamic parameters were calculated  
163 using the standard thermodynamic equation:

$$164 -RT \ln K_a = \Delta G = \Delta H - T \Delta S.$$

165

### 166 **Microscale Thermophoresis (MST)**



167 MST measurement was carried out using a Monolith NT115 (NanoTemper Technologies  
168 GmbH, München, Germany) at 25 °C, 20% LED power and 40 % MEST power as detailed in  
169 Supporting Information. Data analysis was performed with MO Affinity software 2.1  
170 (Nanotemper). The Hill equation was chosen to determine a value for EC50 [30]. EC50 is the  
171 half-maximal effective concentration, meaning the more affinity for the substrate is, the  
172 smaller the value of the EC50 will be.

173

#### 174 **Nuclear Magnetic Resonance (NMR)**

175 NMR experiments were performed on a Bruker Avance III HD 800 MHz spectrometer  
176 equipped with a 5 mm quadruple resonance QCI-P (H/P-C/N/D) cryogenically cooled probe  
177 head (Bruker, Billerica, MA, USA) as detailed in Supporting Information. Analysis of the  
178 data and fitting of the chemical-shift perturbation to the standard equation for a saturation  
179 isotherm was performed using SigmaPlot 11.0 (Systat Software, San Jose, CA, USA).

180

#### 181 **Small angle X-ray scattering (SAXS)**

182 SAXS measurements were performed at Laboratoire de Génie Chimique, Toulouse, on the  
183 XEUSS 2.0 bench (Xenocs, Grenoble, France) equipped with a copper internal source  
184 (Genix3D) that produces a X-ray beam (8 keV and  $30 \cdot 10^6 \text{ ph} \cdot \text{s}^{-1}$ ) providing a size resolution  
185 of approximately  $500 \times 500 \text{ }\mu\text{m}$ . Proteins were concentrated to approximately 10 mg/mL  
186 using a centrifugal filter device (Amicon® Ultra 30 or 50K, Merck KGaA). To remove  
187 aggregates and obtain a monodisperse solution, samples (50  $\mu\text{L}$ ) were injected onto a size  
188 exclusion column mounted on a HPLC coupled to the SAXS. For direct analysis, sample  
189 aliquots (40  $\mu\text{L}$ ) were transferred from the sample holder (maintained at 18 °C using a  
190 circulating water bath) to the measurement cell placed under vacuum to limit air absorption.  
191 Data were collected on a  $150 \times 150 \text{ mm}$  area DECTRIS detector (Pilatus 1M) at a sample-

192 detector distance of 1.216 m, thus procuring a measurement range from 0.005 to 0.5 Å<sup>-1</sup>.  
193 Each sample dataset is an average of at least 6 measurements with a data collection time of  
194 1,800 s. The averaged curves obtained using direct injection and SEC-HPLC were merged to  
195 obtain a composite curve devoid of an aggregation contribution at small angles and displaying  
196 low noise at high angles. Finally, to obtain the absolute scattering intensity I(q) for the  
197 solutes, the background buffer solution contribution was subtracted from the total SAXS  
198 profile. Data integration and reduction were performed using FOXTROT software. The  
199 biophysical parameters, such as gyration radius (R<sub>g</sub>), maximal distance (D<sub>max</sub>) and Porod  
200 volume were calculated using PRIMUS [28] from the ATSAS suite. Low resolution shapes  
201 were calculated with DAMMIF and rigid body molecular modelling using the SAXS data was  
202 performed using CORAL.

203

204 **Paraffin embedding, microtomy, on-section enzymatic digestion and double**  
205 **immunofluorescence labelling.**

206 Sample preparation was performed essentially as previously described [29] with minor  
207 modifications. Briefly, wheat straw (1 cm long) and wheat bran were fixed in acetic  
208 acid/ethanol without aldehyde, infiltrated in paraplast and assembled as tissue arrays in  
209 paraplast. Tissue arrays corresponded to hundreds of wheat bran fragments and at least four  
210 wheat straw cross sections. Tissue array blocks were soaked for several weeks in acetic  
211 acid/ethanol softening solution at 4 °C [30] and 14 µm thick serial sections were displayed on  
212 silane coated slides. Individual slides were dewaxed and covered with a microincubation  
213 chamber (22×40×0.2 mm deep; (200 µL), #70324-20, Electron Microscopy Science, Hatfield,  
214 PA, USA) containing either 50 mM sodium-phosphate 12 mM citrate buffer pH 6 alone or  
215 containing enzymes (300 nM final concentration). Slides were incubated for 24 h at 37 °C in a  
216 humid atmosphere and then recombinant enzymes were digested with proteinase K (5 µg/ml

217 in 0.1 M Tris-HCl pH 8-50 mM EDTA pH 8) for 30 min at 37 °C. Double  
218 immunofluorescence labelling was performed as previously described [31] using xylan-  
219 specific LM11 monoclonal antibody (PlantProbes, Leeds, UK) and cellulose specific His<sub>6</sub>-  
220 Tagged CtCBM3a recombinant protein (PlantProbes, Leeds, UK) as primary probes. These  
221 were labelled with goat anti-rat IgG-Alexa Fluor 488 (ThermoFischer, Waltham, MA, USA)  
222 and His<sub>6</sub>-Tag monoclonal antibody (4E3D10H2/E3)-Alexa Fluor 555 (ThermoFischer,  
223 Waltham, MA, USA), respectively. Slides were mounted in ProLong™ Gold Antifade  
224 mounting medium (ThermoFischer, Waltham, MA, USA) and scanned with a Nanozoomer  
225 2.0 RS scanner (Hamamatsu photonics, Hamamatsu City, Japan) using a 40x objective and  
226 7×1 μm Z stacks. Scans were analysed with NDP view (Hamamatsu photonics). The lignin  
227 autofluorescence observed for the A488 channel in all the cell walls from the  
228 untreated/unlabelled sections was set to a minimum threshold to observe the LM11/A488  
229 specific labelling on the other sections. No such an autofluorescence is seen for the A555  
230 channel. Figures were assembled using Photo-paint (Corel draw graphics suite 2018, Corel,  
231 Ottawa, Canada).

232

## 233 **Results and Discussion**

234

### 235 **Investigating the impact of alternative multidomain arrangements on biological activity**

236 In previous work [25] it was demonstrated how Jo and In can be used to conveniently link  
237 proteins together [24]. Therefore, Jo and In were exploited to create a series of GH-CBM  
238 chimeric proteins based on *NpXyn11A*. The expression of His<sub>6</sub>-tagged *NpXyn11A* linked to  
239 either Jo or In at its *N*-terminus [27] yielded active enzymes. Data regarding In-*NpXyn11A* is  
240 already available [27] so work was restricted to the comparison of the kinetic parameters of  
241 Jo-*NpXyn11A* with those of wild type *NpXyn11A* (Supplementary Table S3). Values of  $K_M$

242  $k_{app}$  for In-*NpXyn11A* and Jo-*NpXyn11A* (1.8 mg.mL<sup>-1</sup> and 2.76 mg.mL<sup>-1</sup>) are 2.4- and 3.7-  
243 fold higher than that of the wild type enzyme (0.75 mg.mL<sup>-1</sup>), indicating that the affinity for  
244 BWX is lowered. As discussed previously [25], additions at the *N*-terminal extremity of the  
245 *NpXyn11A* probably hinder the flexible loops that connect the  $\beta$ -sheets and form the catalytic  
246 pocket that accommodates glycone moieties. This is inferred by the fact that even subtle  
247 modifications in this highly conserved region lead to significant alterations in enzyme activity  
248 [32]. SAXS data (see Figure 3 below) revealed that in solution In-*NpXyn11A*, displayed a  
249 partially unfolded conformation compared to *NpXyn11A*. These observations can possibly be  
250 correlated with the relatively high value of the standard deviation of the kinetic parameters.  
251 Despite changes to  $K_{Mapp}$  and  $k_{cat}$ , the overall catalytic efficiency of the two chimeric enzymes  
252 and *NpXyn11A* were similar due to compensatory effects on  $k_{cat}$  and  $K_{Mapp}$ .

253

254 To use the Jo-In system to assess rapidly the effect of covalent linkage of *NpXyn11A* to  
255 *CtCBM3a* and *CfCBM2b-1*, the same strategy was used to prepare CBM chimeras, yielding  
256 the proteins Jo-CBM3a, In-CBM3a, Jo-CBM2b-1 and In-CBM2b-1. A pull down assay [33]  
257 performed using insoluble cellulose confirmed the binding ability of *CtCBM3a* and its Jo and  
258 In derivatives (see supporting information for detailed protocol, Supplementary Figure S1).  
259 Further investigation using Isothermal titration calorimetry (ITC) and either regenerated  
260 cellulose (RC) or cellulose nanocrystals (CN) confirmed that *CtCBM3a* showed similar  $K_a$   
261 values in the case of both ligands (see supporting information for detailed protocol,  
262 Supplementary Figure S2). It is noteworthy that ITC data also indicate that the *CtCBM3a*-  
263 ligand interaction is enthalpy-driven, with the entropic component being unfavorable,  
264 consistent with previous data related to CBMs binding to RC [34]. Having demonstrated that  
265 CNs constitute a suitable ligand for *CtCBM3a*, they were used to evaluate the binding  
266 properties of Jo-CBM3a and In-CBM3a using microscale thermophoresis (MST) (see

267 supporting information for detailed protocol, **Table 1** and Supplementary Figure S3). Since  
268 Jo- and In-CBM3a are optimally stable in different buffers, to compare them with *Ct*CBM3a  
269 it was necessary to determine CN EC<sub>50</sub> values for the latter in both buffers. Comparing Jo-  
270 CBM3a with *Ct*CBM3a revealed that the EC<sub>50</sub> values were highly similar (0.21 g.L<sup>-1</sup> and 0.14  
271 g.L<sup>-1</sup>, respectively). However, the EC<sub>50</sub> value characterizing the interaction of In-CBM3a with  
272 CN was 60-fold lower than that of *Ct*CBM3a (0.003 g.L<sup>-1</sup> and 0.18 g.L<sup>-1</sup>, respectively),  
273 indicating a higher affinity of In-CBM3a for CN. In this respect, it is noteworthy that  
274 *Ct*CBM3a binding to CN is only moderately sensitive to buffer changes, because the  
275 difference between the two EC<sub>50</sub> values was only 1.28-fold. Therefore, accounting for buffer  
276 effects, while the appendage of Jo to the *N*-terminal extremity of *Ct*CBM3a has a relatively  
277 minor impact on ligand binding, the appendage of In significantly reinforces it.

278

279 To investigate the ligand binding properties of *Cf*CBM2b-1 and its Jo and In derivatives for  
280 soluble oligosaccharides, NMR was used (see supporting information for detailed protocol).  
281 This revealed that CBM binding to X<sub>6</sub> significantly perturbed the chemical shift of the side  
282 chains NH<sup>ε</sup> signals of two solvent exposed Trp residues (Supplementary Figure S4).  
283 Monitoring these shifts provided a *K<sub>d</sub>* value for the *Cf*CBM2b-1/X<sub>6</sub> interaction (**Table 2**),  
284 with data being in the same order of magnitude as a previously reported value [35].  
285 Determination of the *K<sub>d</sub>* value for X<sub>6</sub> binding to In-CBM2b-1 gave a similar value, but in  
286 identical assay conditions no interaction (i.e. *K<sub>d</sub>* > 10 mM) between Jo-CBM2b-1 and X<sub>6</sub> was  
287 evidenced. The reason for this difference is unknown, but clearly Jo engages in unfavorable  
288 interactions with CBM2b-1 that possibly lead to the steric hindrance of one or more of the  
289 CBM's ligand binding determinants [35].

290

291 In summary, the attachment of Jo or In to the *N*-terminus of *NpXyn11A* yielded an active  
292 xylanase. However, attachment of these elements to the *N*-termini of *CtCBM3a* or *CfCBM2b-*  
293 *1* yielded variable results. The attachment of In increased the binding affinity for both CBMs  
294 (significantly for *CBM3a*) while the attachment of Jo decreased both binding affinities  
295 (drastically for *CBM2b-1*). Nevertheless, despite this it was decided to proceed with the  
296 creation of Jo-In linked multimodular chimeras, because previous work has shown that the  
297 covalent association of Jo and In leads to a stable complex devoid of flexibility [24].  
298 Similarly, it was postulated that any deleterious effects arising from the linkage of either Jo or  
299 In to a CBM might be attenuated once the Jo-In complex is formed.

300

### 301 **Creation and biochemical characterization of multimodular chimeric enzymes**

302 Using the different Jo and In derivatives, four multimodular chimeric xylanases were  
303 prepared and purified (**Figure 1A-B**). As shown by SDS-PAGE, the apparent molecular  
304 weight (MW) of *NpXyn11A*-[Jo-In]-*CBM3a*, *NpXyn11A*-[In-Jo]-*CBM3a*, *NpXyn11A*-[Jo-  
305 In]-*CBM2b-1* and *NpXyn11A*-[In-Jo]-*CBM2b-1* are consistent with predicted values,  
306 obtained by summing the MWs of the individual modules (**Figure 1B**, Supplementary Table  
307 S2).

308

309 Measurement of hydrolytic activity of multimodular chimeric xylanases on *pNP-X<sub>3</sub>*, a  
310 substrate small enough to avoid major interference from the CBM, showed that all the  
311 enzymes display activities in the same order of magnitude as recombinant *NpXyn11A* (**Table**  
312 **3**). The activity of *NpXyn11A*-[In-Jo]-*CBM2b-1* was reduced by 36%, even though In-  
313 *NpXyn11A* displayed almost the same activity as *NpXyn11A*. Conversely, while the  
314 attachment of Jo to *NpXyn11A* led to a 20% reduction in activity on *pNP-X<sub>3</sub>*, adding In-  
315 *CBM2b-1* restored activity to a level almost identical to that of *NpXyn11A*. Moreover, the

316 addition of In-CBM3a was not deleterious (Table 3). These results are consistent with current  
317 knowledge that the presence of CBM appendages does not enhance the activity of GHs on  
318 soluble substrates such as *p*NP-glycosides or short oligosaccharides [36].

319

320 Regarding the activities of the four chimeric multimodular xylanases on soluble polymeric  
321 substrates (RAX, WAX and BWX), the enzymes fall into one of two categories. When In-  
322 *Np*Xyn11A is linked to either of the Jo-CBMs the activity on all three substrates is mostly  
323 lower than *Np*Xyn11A, with CBM2b-1 having the most deleterious effect of up to 66% loss  
324 of activity. This result could be related to the loss of binding properties of Jo-CBM2b-1  
325 (Table 2) and does not follow examples in the literature suggesting that activity enhancement  
326 could be expected [37]. Nevertheless, when Jo-*Np*Xyn11A is linked to either In-CBMs,  
327 activity on the different substrates is mostly increased, with the exception of *Np*Xyn11A-[Jo-  
328 In]-CBM2b-1 on BWX (10% activity loss) (Table 3). Remarkably, the activity of *Np*Xyn11A-  
329 [Jo-In]-CBM3a on RAX was increased by 135% compared to that of *Np*Xyn11A on the same  
330 substrate ( $2.92 \pm 0.04$  mM xylose equivalent and  $1.25 \pm 0.16$  mM xylose equivalent after 15  
331 min of reaction, respectively). Clearly, activity increases related to the presence of CBM2b-1  
332 can be tentatively attributed to the specific ligand binding ability of the CBM. However, the  
333 significant increase correlated with the presence of the cellulose-targeting CBM3a is less  
334 intuitive. Nevertheless, a recent study also revealed that the appendage of a cellulose-specific  
335 CBM family 1 to xylanase *Np*Xyn11C [38] increased catalytic efficiency by 21% on BWX.  
336 The underlying reasons for such activity enhancements is unclear and are often treated  
337 cautiously [39]. The fold and architecture of a xylanase core was proposed to explain the  
338 positive effect of a CBM targeting xylan on the catalytic activity of GH family 11 towards  
339 soluble xylan [37]. In the case of the present results, accounting for the relatively large MW  
340 of the xylan polymers ( $\sim 350$  kDa) [27] and the shape of the chimeric enzyme (see SAXS data

341 below, Figure 5B), it may be postulated that non-specific interactions cannot be excluded,  
342 although with no evidence for this.

343

344 The enzymatic activity of *NpXyn11A* derivatives was also evaluated using destarched wheat  
345 bran (DWB), which displays a high arabinoxylan:cellulose ratio [40] and wheat straw (WS),  
346 which conversely displays a low arabinoxylan:cellulose ratio [41]. After 23 h, chimeric  
347 xylanases had released ~7.5-fold more reducing sugars from DWB than from WS (**Figure 2**),  
348 consistent with the greater availability of arabinoxylan in the former and also the greater  
349 structural and chemical complexity of WS. Moreover, the presence of either CBM clearly  
350 enhanced final reducing sugar yield (by ~17% in the case of DWB), even with the presence of  
351 *CtCBM3a* that apparently reduced the initial reaction rate (Figure 2A). The impact of the  
352 nature of the Jo-In linkage was also significant with *NpXyn11A*-[Jo-In]-CBM2b-1 displaying  
353 a faster initial rate than *NpXyn11A*-[In-Jo]-CBM2b-1. On WS, the presence of *CtCBM3a*  
354 proved to be a severe handicap, because activity was ~75% lower than that of the catalytic  
355 domain alone (Figure 2B). Instead, the impact of *CtCBM2b-1* was imperceptible, since the  
356 activities of the *CtCBM2b-1* chimeras were nearly identical to that of the catalytic domain  
357 alone. However, the discriminating nature of the Jo-In linkage was again perceptible, because  
358 despite its faster initial rate, *NpXyn11A*-[In-Jo]-CBM2b-1 generated ~15 % less reducing  
359 sugars when compared to *NpXyn11A*-[Jo-In]-CBM2b-1. These results demonstrate the  
360 importance of substrate targeting by CBMs, especially in complex environments such as  
361 PCWs [15]. DWB provides *CfCBM2b-1* with an abundant source of highly accessible ligand  
362 binding sites, whereas the cellulose-specific *CtCBM3a* probably hinders the early progression  
363 of the enzyme in this matrix. In contrast, WS provides *CtCBM3a* with abundant crystalline  
364 cellulose. Thus, binding of *CtCBM3a* chimeras to cellulose sequesters the enzyme and  
365 prevents it from reaching its arabinoxylan target substrate [15,42]. It is noteworthy that



366 although MST and NMR measurements revealed that In-CBM3a and Jo-CBM2b-1 display  
367 impaired ligand binding (Tables 1 and 2) and experiments using purified xylan substrates  
368 suggest that the activities of *NpXyn11A* chimeras are sensitive to the exact nature of the Jo-In  
369 linkage (Table 3), these factors did not appear to be major determinants of activity on  
370 complex insoluble substrates.

371

### 372 **SAXS and NMR analysis of the multimodular xylanases**

373 As previously described [24], the anti-parallel organization of the stable complex Jo-In and  
374 the possibility to link Jo or In to the *N*- and *C*-termini of proteins of interest [25] offers the  
375 ability to create chimeric proteins and modulates the relative spatial orientation of linked  
376 protein domains. To examine the structures of the protein chimeras created in this work,  
377 SAXS data (**Figure 3**) were recorded and biophysical parameters were extracted (Figure 3C).  
378 The single domain *NpXyn11A* generated a SAXS curve typical of a globular, folded protein  
379 (Figure 3A) that fits well with the theoretical curve calculated using CRY SOL and crystal  
380 structure data (PDB id: 2C1F) (data not shown). However, addition of the In domain resulted  
381 in a modified solution structure, with the  $R_g$  and  $D_{max}$  values (46.2Å and 160Å respectively)  
382 being considerably higher than those of *NpXyn11A* (18.5Å and 60Å respectively), in  
383 agreement with the increase of the MW. It appears that the In domain of In-*NpXyn11A* is  
384 present as a long unfolded tail, while the *NpXyn11A* maintains its globular structure. SAXS  
385 curves of Jo and In derivatives of *CjCBM2b-1* displayed the characteristics of unfolded  
386 proteins with a constant decreased at medium angles (0.008 to 0.1Å<sup>-1</sup>). The proton NMR  
387 spectrum of the isolated *CjCBM2b-1* is characteristic of a well-folded protein domain, with  
388 several methyl resonances below 0 ppm and well-defined Trp side chain signals (**Figure 4**).  
389 The Jo-CBM2b-1 and In-CBM2b-1 constructs display similar resonances devoid of chemical  
390 shifts or spectral broadening, indicating that the CBM domain maintains its 3D fold within

391 these constructs. Indeed, calculation of a difference spectrum (i.e. subtracting the spectrum of  
392 the isolated *Cf*CBM2b-1 domain from that of the Jo/In derivatives) confirmed that the spectra  
393 of the Jo/In -attached *Cf*CBM2b-1 are simple composites of the spectra of the constituent  
394 proteins domains. This implies that when linked to *Cf*CBM2b-1, neither Jo nor In intrinsically  
395 alter the structure of the CBM. However, the fact that Jo-CBM2b-1 binds less effectively than  
396 *Cf*CBM2b-1 to X<sub>6</sub> (Table 2) suggests that the unstructured Jo domain obstructs access to the  
397 CBM's ligand binding site. A similar conclusion possibly explains the lower activity of In-  
398 *Np*Xyn11A against BWX, since the SAXS data (Figure 3) indicates that the In domain is  
399 partially unstructured and might obstruct access to the catalytic site (Supplementary Table S3  
400 and Table 3).

401 The second set of SAXS curves presented in Figure 3B are those of the multimodular  
402 xylanases. These display a similar profile, with intensity decreasing to a plateau at small  
403 angles ( $q < 0.01 \text{ \AA}^{-1}$ ), corresponding to the Guinier region. At higher angles ( $0.01 < q < 0.08 \text{ \AA}^{-1}$   
404 and  $0.08 < q < 0.2 \text{ \AA}^{-1}$ ) the curves decay, consistent with the power law function  $I(q) = q^p$ , with  
405  $p$  value  $\approx 2$  and 4 respectively. This is characteristic of elongated proteins. For the  
406 multimodular xylanases, *Np*Xyn11A-[In-Jo]-CBM2b-1 and *Np*Xyn11A-[Jo-In]-CBM2b-1,  
407 the plots of  $P(r)$  versus  $r$  are very similar (**Figure 5A**) and reflect a multidomain, elongated,  
408 global form (Figure 5B). In contrast, although the  $P(r)$  profiles of *Np*Xyn11A-[In-Jo]-CBM3a  
409 and *Np*Xyn11A-[Jo-In]-CBM3a are also highly similar, they nevertheless differ from those of  
410 *Np*Xyn11A-[In-Jo]-CBM2b-1 and *Np*Xyn11A-[Jo-In]-CBM2b-1, displaying more marked  
411 oscillations that reflect the larger size of *Ct*CBM3a (17.1 kDa compared to 9.1 kDa for  
412 CBM2b-1). Despite this difference, the curves are also indicative of elongated shapes  
413 composed of distinct domains (Figure 5B). The comparison of experimental SAXS data  
414 acquired for *Np*Xyn11A-[In-Jo]-CBM2b-1 and *Np*Xyn11A-[Jo-In]-CBM2b-1 with that of  
415 model curves generated using crystallographic data revealed that these were highly similar,

416 with a goodness of fit  $\chi^2 = 1.25$  and  $1.57$  respectively (**Figure 6A**). For each chimera,  
417 modelling and superimposing the theoretical structure that displayed the best  $\chi^2$  value  
418 provided low-resolution hypothetical structures (Figure 6B-C). Irrespective of the Jo-In  
419 configuration, the distance between *NpXyn11A* and *CfCBM2b-1* is quite similar in both  
420 models ( $118.0 \pm 9.6 \text{ \AA}$  for *NpXyn11A*-[In-Jo]-CBM2b-1 and  $120.6 \pm 5.5 \text{ \AA}$  for *NpXyn11A*-  
421 [Jo-In]-CBM2b-1). However, due to the axial asymmetry in the Jo-In complex, the torsion  
422 angle is  $+66.3 \pm 27.6^\circ$  for *NpXyn11A*-[In-Jo]-CBM2b-1 and  $-145.4 \pm 21.1^\circ$  for *NpXyn11A*-  
423 [Jo-In]-CBM2b-1 (Supplementary Figure S6). Predictive structural modelling of *NpXyn11A*-  
424 [In-Jo]-CBM3a and *NpXyn11A*-[Jo-In]-CBM3a using CORAL was not possible because of  
425 significant structural variability (i.e.  $\chi^2 > 2$ ) that prevented fitting to the molecular envelope of  
426 the SAXS data.

#### 427 **Differences in targeting multimodular xylanases in wheat straw**

428 To further test the possibility of using the chimeric xylanases on raw substrate, experiments  
429 were performed *in situ* on wheat bran and wheat straw PCW sections and the accessible  
430 xylans and cellulose localization were monitored using immunological labelling. Following  
431 treatment of the wheat bran PCW sections with multimodular enzymes (*NpXyn11A*-[Jo-In]-  
432 CBM3a was omitted from this study), LM11/A488-specific xylan labelling between the  
433 pericarp and the nucellar epidermis (**Figure 7 C1-F1**) and intense continuous CBM3a/A555-  
434 specific labelling of the nucellar epidermis (Figure 7 C2-F2) were observed. This contrasts  
435 with the untreated sections that displayed no LM11/A488 labelling and only faint  
436 CBM3a/A555 labelling (Figure 7B). Although increased labelling after enzymatic treatment  
437 appears counter intuitive, it is almost certainly a consequence of PCW complexity. The action  
438 of the chimeric xylanases leads to the removal of xylan and concomitant exposure of hitherto  
439 masked PCW components, such as cellulose and xylan, which constitute new ligands for  
440 antibody or CBM binding. However, experiments performed on DWB failed to reveal any

441 major changes to labelling. Therefore, subsequent work focused on WS (**Figure 8**,  
442 Supplementary Figures S7 and S8). The use of either probe on untreated sections produced  
443 homogenous labelling of both PCW components (Figure 8B). However, after treatment with  
444 *NpXyn11A* (Figure 8C) and *NpXyn*-[Jo-In]-CBM2b-1 (Figure 8D), LM11/A488 labelling  
445 was repeatedly found to be diminished when observing different vascular bundles  
446 (Supplementary Figure S7). This suggests that the presence of CBM2b-1 did not enhance the  
447 activity of *NpXyn11A* on WS. Additionally, compared to *NpXyn11A*, *NpXyn*-[Jo-In]-  
448 CBM2b-1 was apparently less active on intervascular fibres. Finally, diminution of the  
449 CBM3a/A555 labelling (cellulose-specific probe) was correlated with xylan hydrolysis.  
450 Conversely, treatment with *NpXyn11A*-[In-Jo]-CBM2b-1 or *NpXyn11A*-[In-Jo]-CBM3a  
451 generally did not affect LM11/A488 labelling intensity (Figure 8E-F; Supplementary Figure  
452 S7), although this was strongly enhanced in patches around the phloem, the protoxylem and in  
453 vascular bundle cell corners. In distal zones, intense patches of LM11/A488 labelling were  
454 also observed in sclerenchyma cell corners and around the pith parenchyma intercellular  
455 spaces (Supplementary Figure S8). For PCW sections treated with *NpXyn11A*-[In-Jo]-  
456 CBM2b-1, additional patches of LM11/A488 labelling were also observed in the intervascular  
457 fibres, but this was not the case when *NpXyn11A*-[In-Jo]-CBM3a was used (Figure 8E-F;  
458 Supplementary Figure S7). The impact on cellulose labelling was also more evident for  
459 *NpXyn11A*-[In-Jo]-CBM2b-1 than for *NpXyn11A*-[In-Jo]-CBM3a (Figure 8E-F;  
460 Supplementary Figure S7).

461

462 Previously, both *CtCBM3a* and *CfCBM2b-1* were shown to potentiate the activity of a  
463 cognate xylanase on tobacco PCWs, presumably by improving its substrate targeting  
464 capability [15]. However, the present results do not confirm this and may signify limited  
465 usefulness for the Jo-In system when studying enzyme activity on complex matrices, even

466 though the structural environment of xylan and xylan-cellulose interactions are different in  
467 tobacco PCW [43]. It can be postulated that Jo-In introduces a high degree of rigidity  
468 compared to natural linkers found in PCW-degrading enzymes. While rigidity might be  
469 undesirable in certain circumstances, it can be useful in others. Specifically, greater protein  
470 rigidity will be useful in investigating different spatial organizations in multidomain proteins,  
471 locking chimeric protein isoforms in different domain configurations.

472

### 473 **Conclusions**

474 A previous study on *Ct*CBM3a linked to endoglucanase CelA of *Clostridium*  
475 *thermocellum* revealed that the CBM must be correctly oriented to potentiate enzymatic  
476 activity, especially on insoluble substrates [44]. In this regard, the nature of the linker is  
477 certainly important because its structure will strongly contribute to the spatial orientations of  
478 linked protein domains. Here, the Jo-In complex has been used to link protein domains, the  
479 resultant linker complexes being stable, rather rigid protein structures. The first implication of  
480 this rigidity is the likelihood that there will be no physical interference between the attached  
481 protein domains. In the case of *Np*Xyn11A linked to CBMs, this is certainly the case because  
482 the solution structures are elongated and characterized by well separated GH and CBM  
483 domains. The second implication is that the spatial orientation (torsion angle) of the two  
484 linked proteins domains is locked. If this is optimal then synergy should be possible and  
485 enhancement of the activity of the GH domain will be a likely outcome. Conversely, if this is  
486 suboptimal, the chimera will be definitively impaired, lacking sufficient linker flexibility to  
487 allow alternative solution conformers. Accordingly, it is proposed that data related to the  
488 hydrolysis of insoluble substrates described herein reflects this fact, revealing that  
489 *Np*Xyn11A-[Jo-In]-CBM2b-1 has a more optimal configuration for hydrolysis than  
490 *Np*Xyn11A-[In-Jo]-CBM2b-1. The third implication of linker rigidity is that protein chimeras

491 are likely to encounter difficulty in penetrating structurally complex three-dimensional  
492 matrices. In this work, the fact that the addition of CBMs to *NpXyn11A* failed to potentiate  
493 the hydrolysis of wheat straw possibly supports this hypothesis.

494 In summary, this work confirms the usefulness of the Jo-In system in creating  
495 multidomain GHs. However, one caveat is the intrinsic rigidity of Jo-In. When designing  
496 chimeric proteins, this property must be considered with respect to the intended purpose.

497

#### 498 **Acknowledgements**

499 We thank Pr. Harry Gilbert (ICMB, Newcastle University) for providing access and expertise  
500 in ITC experiments. We also thank Dr. Jean Jacques Bono and Virginie Gascioli (LIPM,  
501 Toulouse) for providing access and expertise in MST experiments. The imaging using  
502 Nanozoomer RS was performed at the FR-AIB imaging platform of TRI-genotoul facility  
503 (Toulouse). We thank Dr. Gianluca Cioci for technical assistance with FPLC provided by the  
504 ICEO facility dedicated to enzyme screening and discovery, part of the Integrated Screening  
505 Platform of Toulouse (PICT, IBiSA).

506

#### 507 **Author contributions**

508 LB, VB, CYM conceived and designed the experiments. LB, PR, TE, GL, IV and CYM  
509 performed the experiments. LB, VB, PR, GL, MJO and CYM analyzed the data. LB, MJO  
510 and CYM wrote the paper.

511

#### 512 **References**

513 [1] Wang Y, Zhang H, Zhong H, Xue Z. Protein domain identification methods and online  
514 resources. *Comput Struct Biotechnol J* 2021;19:1145–53.  
515 <https://doi.org/10.1016/j.csbj.2021.01.041>.

- 516 [2] Apic G, Gough J, Teichmann SA. Domain combinations in archaeal, eubacterial and  
517 eukaryotic proteomes. *J Mol Biol* 2001;310:311–25.  
518 <https://doi.org/10.1006/jmbi.2001.4776>.
- 519 [3] Apic G, Huber W, Teichmann SA. Multi-domain protein families and domain pairs:  
520 comparison with known structures and a random model of domain recombination. *J*  
521 *Struct Funct Genomics* 2003;4:67–78. <https://doi.org/10.1023/A:1026113408773>.
- 522 [4] Altschuh D, Tessier DC, Vernet T. Modulation of the enzymatic activity of papain by  
523 interdomain residues remote from the active site. *Protein Eng Des Sel* 1994;7:769–76.  
524 <https://doi.org/10.1093/protein/7.6.769>.
- 525 [5] Valentini G, Chiarelli L, Fortin R, Speranza ML, Galizzi A, Mattevi A. The Allosteric  
526 Regulation of Pyruvate Kinase. *J Biol Chem* 2000;275:18145–52.  
527 <https://doi.org/10.1074/jbc.M001870200>.
- 528 [6] Lombard V, Golaconda Ramulu H, Drula E, Coutinho PM, Henrissat B. The  
529 carbohydrate-active enzymes database (CAZy) in 2013. *Nucleic Acids Res*  
530 2014;42:D490–5. <https://doi.org/10.1093/nar/gkt1178>.
- 531 [7] Amos RA, Mohnen D. Critical review of plant cell wall matrix polysaccharide  
532 glycosyltransferase activities verified by heterologous protein expression. *Front Plant*  
533 *Sci* 2019;10. <https://doi.org/10.3389/fpls.2019.00915>.
- 534 [8] Wu H, Ioannou E, Henrissat B, Montanier CY, Bozonnet S, O’Donohue MJ, et al.  
535 Multimodularity of a GH10 Xylanase Found in the Termite Gut Metagenome. *Appl*  
536 *Environ Microbiol* 2021;87. <https://doi.org/10.1128/AEM.01714-20>.
- 537 [9] Henrissat B, Davies GJ. Glycoside Hydrolases and Glycosyltransferases. Families,  
538 Modules, and Implications for Genomics. *Plant Physiol* 2000;124:1515–9.  
539 <https://doi.org/10.1104/pp.124.4.1515>.
- 540 [10] Shoseyov O, Shani Z, Levy I. Carbohydrate binding modules: biochemical properties

- 541 and novel applications. *Microbiol Mol Biol Rev* 2006;70:283–95.  
542 <https://doi.org/10.1128/MMBR.00028-05>.
- 543 [11] Sammond DW, Payne CM, Brunecky R, Himmel ME, Crowley MF, Beckham GT.  
544 Cellulase linkers are optimized based on domain type and function: insights from  
545 sequence analysis, biophysical measurements, and molecular simulation. *PLoS One*  
546 2012;7:e48615. <https://doi.org/10.1371/journal.pone.0048615>.
- 547 [12] Sidar A, Albuquerque ED, Voshol GP, Ram AFJ, Vijgenboom E, Punt PJ.  
548 Carbohydrate binding modules: diversity of domain architecture in amylases and  
549 cellulases from filamentous microorganisms. *Front Bioeng Biotechnol* 2020;8.  
550 <https://doi.org/10.3389/fbioe.2020.00871>.
- 551 [13] Pasari N, Adlakha N, Gupta M, Bashir Z, Rajacharya GH, Verma G, et al. Impact of  
552 Module-X2 and Carbohydrate Binding Module-3 on the catalytic activity of associated  
553 glycoside hydrolases towards plant biomass. *Sci Rep* 2017;7:3700.  
554 <https://doi.org/10.1038/s41598-017-03927-y>.
- 555 [14] Cuskin F, Flint JE, Gloster TM, Morland C, Basle A, Henrissat B, et al. How nature  
556 can exploit nonspecific catalytic and carbohydrate binding modules to create enzymatic  
557 specificity. *Proc Natl Acad Sci* 2012;109:20889–94.  
558 <https://doi.org/10.1073/pnas.1212034109>.
- 559 [15] Herve C, Rogowski A, Blake AW, Marcus SE, Gilbert HJ, Knox JP. Carbohydrate-  
560 binding modules promote the enzymatic deconstruction of intact plant cell walls by  
561 targeting and proximity effects. *Proc Natl Acad Sci* 2010;107:15293–8.  
562 <https://doi.org/10.1073/pnas.1005732107>.
- 563 [16] Shah NH, Muir TW. Inteins: nature’s gift to protein chemists. *Chem Sci* 2014;5:446–  
564 61. <https://doi.org/10.1039/C3SC52951G>.
- 565 [17] Pinto F, Thornton EL, Wang B. An expanded library of orthogonal split inteins enables



566 modular multi-peptide assemblies. *Nat Commun* 2020;11:1529.  
567 <https://doi.org/10.1038/s41467-020-15272-2>.

568 [18] Zhao X, Scheffner M, Marx A. Assembly of branched ubiquitin oligomers by click  
569 chemistry. *Chem Commun* 2019;55:13093–5. <https://doi.org/10.1039/C9CC07303E>.

570 [19] You C, Piehler J. Multivalent chelators for spatially and temporally controlled protein  
571 functionalization. *Anal Bioanal Chem* 2014;406:3345–57.  
572 <https://doi.org/10.1007/s00216-014-7803-y>.

573 [20] Singh S, Kluger R. Self-Assembly of a Functional Triple Protein: Hemoglobin-Avidin-  
574 Hemoglobin via Biotin–Avidin Interactions. *Biochemistry* 2016;55:2875–82.  
575 <https://doi.org/10.1021/acs.biochem.6b00215>.

576 [21] Fierobe H-P, Mechaly A, Tardif C, Belaich A, Lamed R, Shoham Y, et al. Design and  
577 Production of Active Cellulosome Chimeras. *J Biol Chem* 2001;276:21257–61.  
578 <https://doi.org/10.1074/jbc.M102082200>.

579 [22] Sun F, Zhang W-B. Unleashing chemical power from protein sequence space toward  
580 genetically encoded “click” chemistry. *Chinese Chem Lett* 2017;28:2078–84.  
581 <https://doi.org/10.1016/j.ccllet.2017.08.052>.

582 [23] Zakeri B, Fierer JO, Celik E, Chittock EC, Schwarz-Linek U, Moy VT, et al. Peptide  
583 tag forming a rapid covalent bond to a protein, through engineering a bacterial adhesin.  
584 *Proc Natl Acad Sci* 2012;109:E690–7. <https://doi.org/10.1073/pnas.1115485109>.

585 [24] Bonnet J, Cartannaz J, Tourcier G, Contreras-Martel C, Kleman JP, Morlot C, et al.  
586 Autocatalytic association of proteins by covalent bond formation: a Bio Molecular  
587 Welding toolbox derived from a bacterial adhesin. *Sci Rep* 2017;7:43564.  
588 <https://doi.org/10.1038/srep43564>.

589 [25] Enjalbert T, De La Mare M, Roblin P, Badruna L, Vernet T, Dumon C, et al.  
590 Characterisation of the effect of the spatial organisation of hemicellulases on the

591 hydrolysis of plant biomass polymer. *Int J Mol Sci* 2020;21:4360.  
592 <https://doi.org/10.3390/ijms21124360>.

593 [26] Vardakou M, Dumon C, Murray JW, Christakopoulos P, Weiner DP, Juge N, et al.  
594 Understanding the structural basis for substrate and inhibitor recognition in eukaryotic  
595 GH11 xylanases. *J Mol Biol* 2008;375:1293–305.  
596 <https://doi.org/10.1016/j.jmb.2007.11.007>.

597 [27] Montanier CY, Fanuel M, Rogniaux H, Ropartz D, Di Guilmi A-M, Bouchoux A.  
598 Changing surface grafting density has an effect on the activity of immobilized xylanase  
599 towards natural polysaccharides. *Sci Rep* 2019;9:5763. [https://doi.org/10.1038/s41598-](https://doi.org/10.1038/s41598-019-42206-w)  
600 [019-42206-w](https://doi.org/10.1038/s41598-019-42206-w).

601 [28] Konarev P V., Volkov V V., Sokolova A V., Koch MHJ, Svergun DI. PRIMUS : a  
602 Windows PC-based system for small-angle scattering data analysis. *J Appl Crystallogr*  
603 2003;36:1277–82. <https://doi.org/10.1107/S0021889803012779>.

604 [29] Badruna L, Burlat V, Montanier CY. CBMs as probes to explore plant cell wall  
605 heterogeneity using immunocytochemistry, 2017, p. 181–97.  
606 [https://doi.org/10.1007/978-1-4939-6899-2\\_14](https://doi.org/10.1007/978-1-4939-6899-2_14).

607 [30] Brandizzi F. *Plant microtechnique and microscopy*. vol. 86. 2000.  
608 <https://doi.org/10.1006/anbo.2000.1231>.

609 [31] Francoz E, Ranocha P, Le Ru A, Martinez Y, Fourquaux I, Jauneau A, et al. Pectin  
610 demethylesterification generates platforms that anchor peroxidases to remodel plant  
611 cell wall domains. *Dev Cell* 2019;48:261-276.e8.  
612 <https://doi.org/10.1016/j.devcel.2018.11.016>.

613 [32] Song L, Siguier B, Dumon C, Bozonnet S, O'Donohue MJ. Engineering better  
614 biomass-degrading ability into a GH11 xylanase using a directed evolution strategy.  
615 *Biotechnol Biofuels* 2012;5:3. <https://doi.org/10.1186/1754-6834-5-3>.

- 616 [33] Crouch LI, Labourel A, Walton PH, Davies GJ, Gilbert HJ. The Contribution of non-  
617 catalytic carbohydrate binding modules to the activity of lytic polysaccharide  
618 monooxygenases. *J Biol Chem* 2016;291:7439–49.  
619 <https://doi.org/10.1074/jbc.M115.702365>.
- 620 [34] Boraston AB. The interaction of carbohydrate-binding modules with insoluble non-  
621 crystalline cellulose is enthalpically driven. *Biochem J* 2005;385:479–84.  
622 <https://doi.org/10.1042/BJ20041473>.
- 623 [35] Simpson PJ, Bolam DN, Cooper A, Ciruela A, Hazlewood GP, Gilbert HJ, et al. A  
624 family IIb xylan-binding domain has a similar secondary structure to a homologous  
625 family IIa cellulose-binding domain but different ligand specificity. *Structure*  
626 1999;7:853–64. [https://doi.org/10.1016/S0969-2126\(99\)80108-7](https://doi.org/10.1016/S0969-2126(99)80108-7).
- 627 [36] Tomme P, Tilbeurgh H, Pettersson G, Damme J, Vandekerckhove J, Knowles J, et al.  
628 Studies of the cellulolytic system of *Trichoderma reesei* QM 9414. Analysis of domain  
629 function in two cellobiohydrolases by limited proteolysis. *Eur J Biochem*  
630 1988;170:575–81. <https://doi.org/10.1111/j.1432-1033.1988.tb13736.x>.
- 631 [37] Kittur FS, Mangala SL, Rus'd AA, Kitaoka M, Tsujibo H, Hayashi K. Fusion of family  
632 2b carbohydrate-binding module increases the catalytic activity of a xylanase from  
633 *Thermotoga maritima* to soluble xylan. *FEBS Lett* 2003;549:147–51.  
634 [https://doi.org/10.1016/S0014-5793\(03\)00803-2](https://doi.org/10.1016/S0014-5793(03)00803-2).
- 635 [38] Zhang Y, Yang H, Yu X, Kong H, Chen J, Luo H, et al. Synergistic effect of acetyl  
636 xylan esterase from *Talaromyces leycettanus* JCM12802 and xylanase from  
637 *Neocallimastix patriciarum* achieved by introducing carbohydrate-binding module-1.  
638 *AMB Express* 2019;9:13. <https://doi.org/10.1186/s13568-019-0740-6>.
- 639 [39] Hoffmam ZB, Zanphorlin LM, Cota J, Diogo JA, Almeida GB, Damásio ARL, et al.  
640 Xylan-specific carbohydrate-binding module belonging to family 6 enhances the

- 641 catalytic performance of a GH11 endo-xylanase. *N Biotechnol* 2016;33:467–72.  
642 <https://doi.org/10.1016/j.nbt.2016.02.006>.
- 643 [40] Bouraoui H, Desrousseaux M-L, Ioannou E, Alvira P, Manai M, Rémond C, et al. The  
644 GH51  $\alpha$ -l-arabinofuranosidase from *Paenibacillus* sp. THS1 is multifunctional,  
645 hydrolyzing main-chain and side-chain glycosidic bonds in heteroxylans. *Biotechnol*  
646 *Biofuels* 2016;9:140. <https://doi.org/10.1186/s13068-016-0550-x>.
- 647 [41] Motte J-C, Escudié R, Beaufils N, Steyer J-P, Bernet N, Delgenès J-P, et al.  
648 Morphological structures of wheat straw strongly impacts its anaerobic digestion. *Ind*  
649 *Crops Prod* 2014;52:695–701. <https://doi.org/10.1016/j.indcrop.2013.11.038>.
- 650 [42] Gao D, Chundawat SPS, Sethi A, Balan V, Gnanakaran S, Dale BE. Increased enzyme  
651 binding to substrate is not necessary for more efficient cellulose hydrolysis. *Proc Natl*  
652 *Acad Sci* 2013;110:10922–7. <https://doi.org/10.1073/pnas.1213426110>.
- 653 [43] Busse-Wicher M, Gomes TCF, Tryfona T, Nikolovski N, Stott K, Grantham NJ, et al.  
654 The pattern of xylan acetylation suggests xylan may interact with cellulose microfibrils  
655 as a twofold helical screw in the secondary plant cell wall of *Arabidopsis thaliana*.  
656 *Plant J* 2014;79:492–506. <https://doi.org/10.1111/tpj.12575>.
- 657 [44] Sajjad M, Khan MIM, Zafar R, Ahmad S, Niazi UHK, Akhtar MW. Influence of  
658 positioning of carbohydrate binding module on the activity of endoglucanase CelA of  
659 *Clostridium thermocellum*. *J Biotechnol* 2012;161:206–12.  
660 <https://doi.org/10.1016/j.jbiotec.2012.05.023>.
- 661 [45] Wilkins MR, Gasteiger E, Bairoch A, Sanchez J-C, Williams KL, Appel RD, et al.  
662 Protein identification and analysis tools in the ExPASy Server. *2-D Proteome Anal.*  
663 *Protoc.*, New Jersey: Humana Press; n.d., p. 531–52. [https://doi.org/10.1385/1-59259-](https://doi.org/10.1385/1-59259-584-7:531)  
664 [584-7:531](https://doi.org/10.1385/1-59259-584-7:531).
- 665 [46] Fumagalli M, Ouhab D, Boisseau SM, Heux L. Versatile gas-phase reactions for

666 surface to bulk esterification of cellulose microfibrils aerogels. *Biomacromolecules*  
667 2013;14:3246–55. <https://doi.org/10.1021/bm400864z>.  
668 [47] Wu H, Montanier CY, Dumon C. Quantifying CBM carbohydrate interactions using  
669 microscale thermophoresis, 2017, p. 129–41. [https://doi.org/10.1007/978-1-4939-6899-](https://doi.org/10.1007/978-1-4939-6899-2_10)  
670 [2\\_10](https://doi.org/10.1007/978-1-4939-6899-2_10).  
671 [48] Kaufmann M, Klinger C, editors. *Functional Genomics*. vol. 815. New York, NY:  
672 Springer New York; 2012. <https://doi.org/10.1007/978-1-61779-424-7>.  
673 [49] Millard P, Lippens G. Interact: Automated analysis of protein-ligand interactions by  
674 1D and 2D NMR. *BioRxiv* 2018:215194. <https://doi.org/10.1101/215194>.

675

676

677

## 678 **Legends to Figures and Tables**

679 **Figure 1:** (A) Representation of the proteins studied in this work. The multimodular enzymes  
680 are linked *via* an isopeptide bond between the Lys191 of Jo and the Asp695 of In (double fine  
681 black line). Although Jo and In are fused at the *N*-termini of *NpXyn11A* and the CBMs  
682 respectively, the covalent Jo-In or In-Jo association between the GH and the CBM is shown in  
683 square brackets for simplicity. (B) SDS-PAGE of the protein used in this study. Lanes: M,  
684 molecular markers; 1, *NpXyn11A*; 2, Jo-*NpXyn11A*; 3, *CtCBM3a*; 4, Jo-CBM3a; 5,  
685 *NpXyn11A*-[In-Jo]-CBM3a; 6, *CfCBM2b-1*; 7, Jo-CBM2b-1; 8, In-CBM2b-1; 9, *NpXyn11A*-  
686 [In-Jo]-CBM2b-1; 10, *NpXyn11A*-[Jo-In]-CBM2b-1. For illustration 11, *NpXyn11A*-[Jo-In]-  
687 CBM3a; 12, In-CBM3a. Original gels are provided in Supplementary Information (Figure  
688 S5).

689

690 **Figure 2.** Degradation of complex substrates by *NpXyn11A* and derivatives thereof. (A)  
691 Wheat bran. (B) Wheat straw. Enzyme reactions were conducted in 50 mM sodium  
692 phosphate, 12 mM sodium citrate pH6, supplemented with 1 mg/ml BSA, at 37°C. Enzyme  
693 loading was at 1  $\mu$ M. Substrate concentration was at 2% w/v.

694

695 **Figure 3:** (A) SAXS data recorded for *NpXyn11A*, In-*NpXyn11A*, In-CBM2b-1 and Jo-  
696 CBM2b-1. (B) SAXS data recorded for *NpXyn11A*-[In-Jo]-CBM2b-1, *NpXyn11A*-[Jo-In]-  
697 CBM2b-1, *NpXyn11A*-[In-Jo]-CBM3a and *NpXyn11A*-[Jo-In]-CBM3a. (C) Table  
698 summarizing all parameters extracted from the Guinier plot and pair-atom distribution  
699 function  $P(r)$  such as gyration radius  $R_g$  and maximum internal distance  $D_{max}$ . The folding  
700 state deduced from the parameters and the shape of the curves are also mentioned in the table  
701 for each fragment.

702

703 **Figure 4:** 1D proton spectrum of (A) isolated *Cf*CBM2b-1 (bottom, black), of In-CBMb2-1  
704 (middle, red) and the difference spectrum (*Cf*CBM2b-1 – In-CBMb2-1) (top, green). (B)  
705 Isolated *Cf*CBM2b-1 (bottom, black), of Jo-CBMb2-1 (middle, red) and the difference  
706 spectrum (*Cf*CBM2b-1 – Jo-CBMb2-1) (top, orange).

707

708 **Figure 5:** (A) Pair distribution function calculated from SAXS data of *NpXyn11A*-[In-Jo]-  
709 CBM2b-1 and *NpXyn11A*-[Jo-In]-CBM2b-1 (blue and red curves respectively) and from  
710 SAXS data of *NpXyn11A*-[In-Jo]-CBM3a and *NpXyn11A*-[Jo-In]-CBM3a (green and yellow  
711 curves respectively). The  $P(r)$  function is plotted as  $P(r)/P_{max}(r)$  vs distance  $r$  in order to  
712 compare the different curves by normalizing with  $P_{max}(r)$ . (B) Low resolution shape  
713 calculated with the DAMMIF program from ATSAS suite for the four constructs. The shapes  
714 are built with Pymol in mesh representation and filled with transparent spheres.

715

716 **Figure 6:** (A) Comparison of experimental curves generated using *NpXyn11A*-[In-Jo]-  
717 CBM2b-1 and *NpXyn11A*-[Jo-In]-InCBM2b-1 and the theoretical curves (dotted black line)  
718 calculated using CRY SOL and crystallographic data. (B) Models of *NpXyn11A*-[In-Jo]-  
719 CBM2b-1 and (C) *NpXyn11A*-[Jo-In]-InCBM2b-1 were calculated using the CORAL  
720 program. In both models, Jo-In are coloured red and green respectively. *NpXyn11A* is in cyan  
721 and *CtCBM2b-1* in yellow. Catalytic residues of *NpXyn11A* and residues involved in ligand  
722 binding recognition of *CtCBM2b-1* are represented by red lines. The domains and the linker  
723 are modelled with Pymol using cartoon and grey sphere representations respectively.

724

725 **Figure 7:** Double immunofluorescence of paraffin-embedded wheat bran serial sections  
726 showing the impact of enzymatic on-section treatment on accessible xylan and cellulose  
727 immunolabelling. Serial sections of wheat bran were incubated for 24 h using the xylanase  
728 derivatives as labelled on the images and further used for double indirect immunofluorescence  
729 using LM11 (xylan specific antibody) and His<sub>6</sub>-CBM3a (cellulose specific CBM) as primary  
730 probes and anti-rat IgG-Alexa 488 and anti-His<sub>6</sub>-Alexa 555, respectively. The individual  
731 fluorescence channels are shown in the two first rows as labelled, and the merge of both  
732 fluorescence channels with the bright field channel is shown in the third row. Arrowheads:  
733 pericarp/nucellar epidermis interface; Bars: 300 μm.

734

735 **Figure 8:** Double immunofluorescence of paraffin-embedded wheat straw serial sections  
736 showing the impact of enzymatic on-section treatment on xylan and cellulose  
737 immunolabelling. Serial sections of wheat straw were incubated for 24 h using the  
738 recombinant xylanase derivatives as labelled on the images and further used for double  
739 indirect immunofluorescence using LM11 (xylan specific antibody) and His<sub>6</sub>-CBM3a

740 (cellulose specific CBM) as primary probes and anti-rat IgG-Alexa 488 and anti-His<sub>6</sub>-Alexa  
741 555, respectively. The individual fluorescence channels are shown as labelled for a wide field  
742 view (two left rows) and for a vascular bundle magnified view (two right rows). Note, that to  
743 enable fair comparison between the treatment/controls, the same zones on the different serial  
744 sections are displayed. Note also that an intermediate magnification is shown for this vascular  
745 bundle in the ROI of Supplementary Figure S7, as well as two additional ROIs. bsf, bundle  
746 sheath fibres; cp, cortical parenchyma zones; ep, epidermis; if, intervascular fibres; mx,  
747 metaxylem; p, pith; ph, phloem; pp, pith parenchyma; px, protoxylem; s, sclerenchyma; vb,  
748 vascular bundle. Bars: 250  $\mu$ m (two left rows); 25  $\mu$ m (two right rows).

749

750

751

752 **Table 1:** Binding affinity of *Ct*CBM3a and derivatives against cellulose nanocrystals. Buffer 1:  
753 50 mM Tris HCl pH 7.4, 150 mM NaCl, 10 mM MgCl<sub>2</sub>, 0.05 % Tween 20. Buffer 2: 50 mM  
754 sodium phosphate buffer, pH 7 and 0.05 % pluronic acid. See Supplementary Figure S3 for  
755 chart. EC<sub>50</sub> is the half-maximal effective concentration, i.e. the higher the affinity for the  
756 substrate, the smaller the value of the EC<sub>50</sub>.

757

758 **Table 2:** Ligand affinities of *Cf*CBM2b-1, *In*-CBM2b-1 and *Jo*-CBM2b-1 for xylohexaose as  
759 measured by 1D NMR by titrating the resonances of the NH $\epsilon$  of Trp 259 and Trp 291.  
760 Experiments were conducted in 50 mM sodium phosphate pH 7 at 298 °K.

761



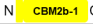






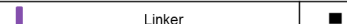




762 **Table 3:** Specific activity of *Np*Xyn11A and derivatives, as single enzymes or in complex.  
763 Reactions were performed in 50 mM sodium phosphate, 12 mM sodium citrate pH 6,  
764 supplemented with 1mg/mL BSA, at 37°C. Substrate concentrations were 5 mM 4-

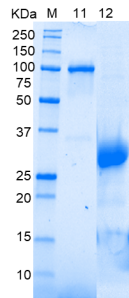
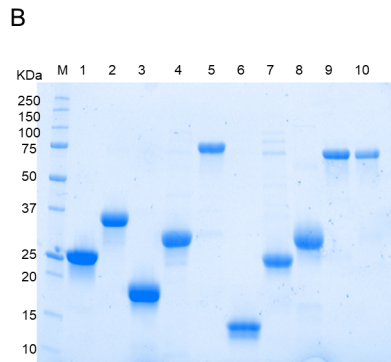


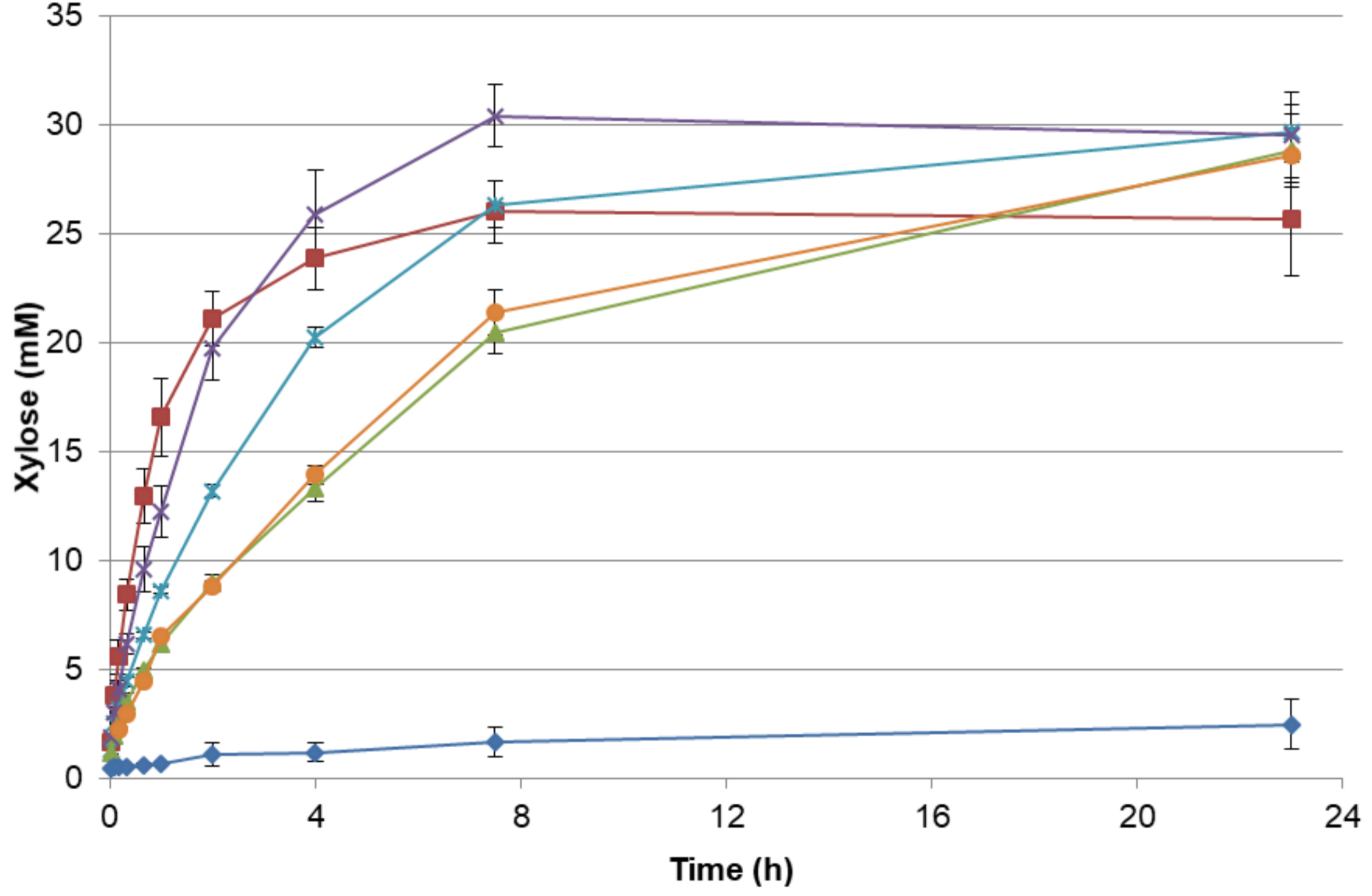
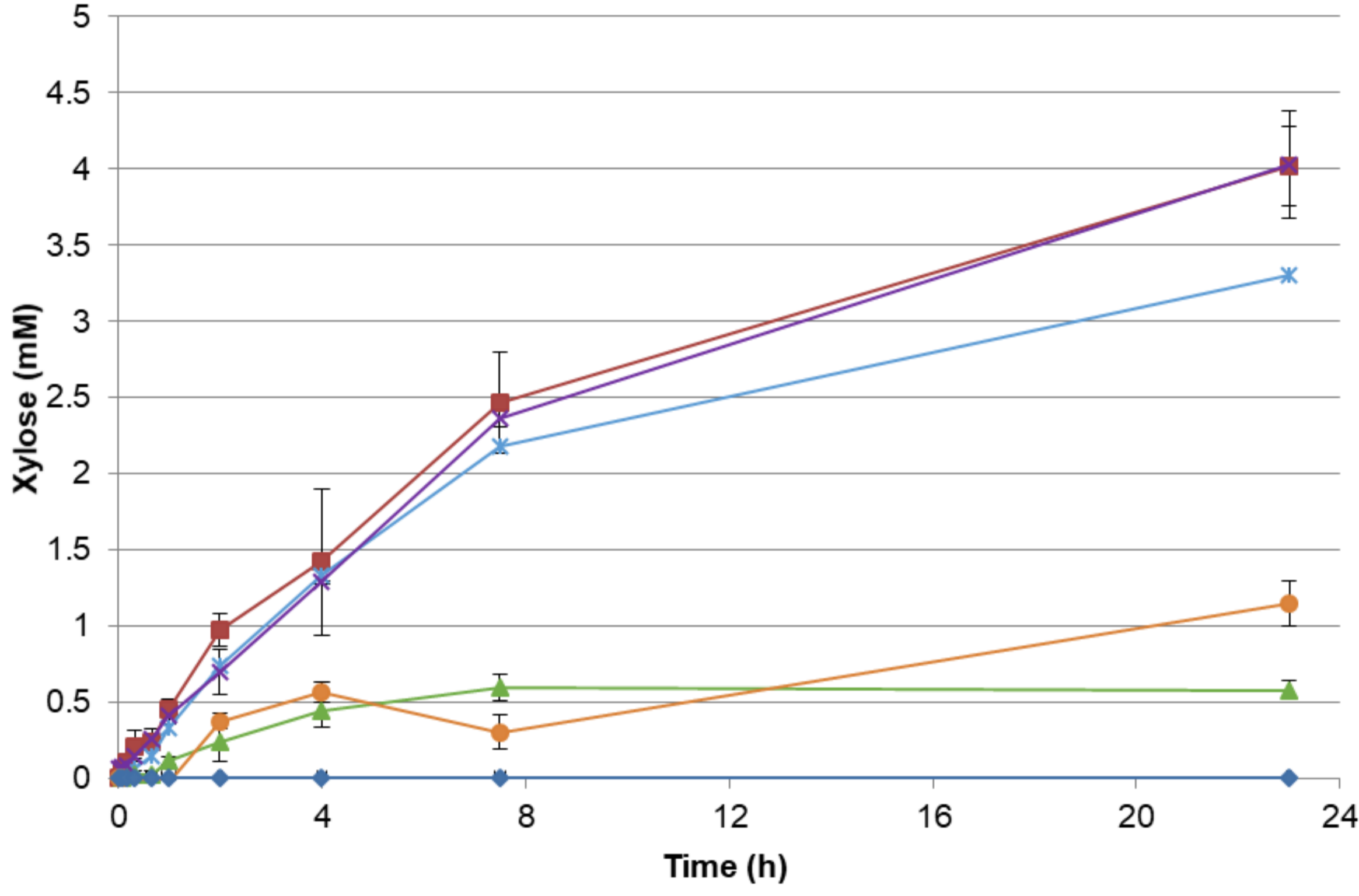
765 nitrophenyl- $\beta$ -D-xylotrioxide (*p*NP-X<sub>3</sub>), 0.5% w/v wheat arabinoxylan (WAX), 0.5% w/v rye  
766 arabinoxylan (RAX) and 1% w/v beechwood xylan (BWV). The values are shown as means  $\pm$   
767 standard deviation of replicate n = 3.

768

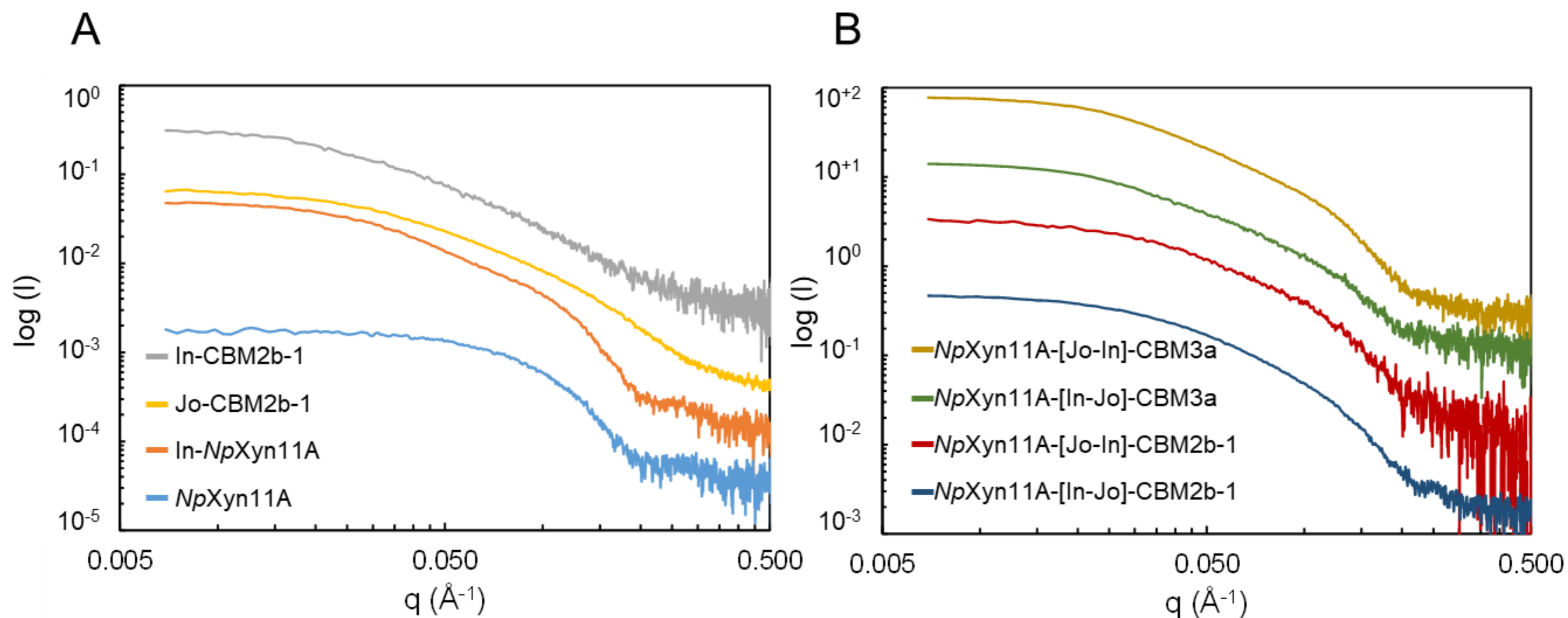
**A**

	Protein name	Protein scheme	Position in Fig.2B
Single proteins	<i>NpXyn11A</i>	N  C	1
	CtCBM3a	N  C	3
	CtCBM2b-1	N  C	6
Jo/In fusion proteins	In- <i>NpXyn11A</i>	N  C	-
	Jo- <i>NpXyn11A</i>	N  C	2
	In-CBM3a	N  C	12
	Jo-CBM3a	N  C	4
	In-CBM2b-1	N  C	8
	Jo-CBM2b-1	N  C	7
	His-Tag		
Multi-modular enzymes	<i>NpXyn11A</i> -[In-Jo]- <i>CBM3a</i>	C  C	5
	<i>NpXyn11A</i> -[Jo-In]- <i>CBM3a</i>	C  C	11
	<i>NpXyn11A</i> -[In-Jo]- <i>CBM2b-1</i>	C  C	9
	<i>NpXyn11A</i> -[Jo-In]- <i>CBM2b-1</i>	C  C	10



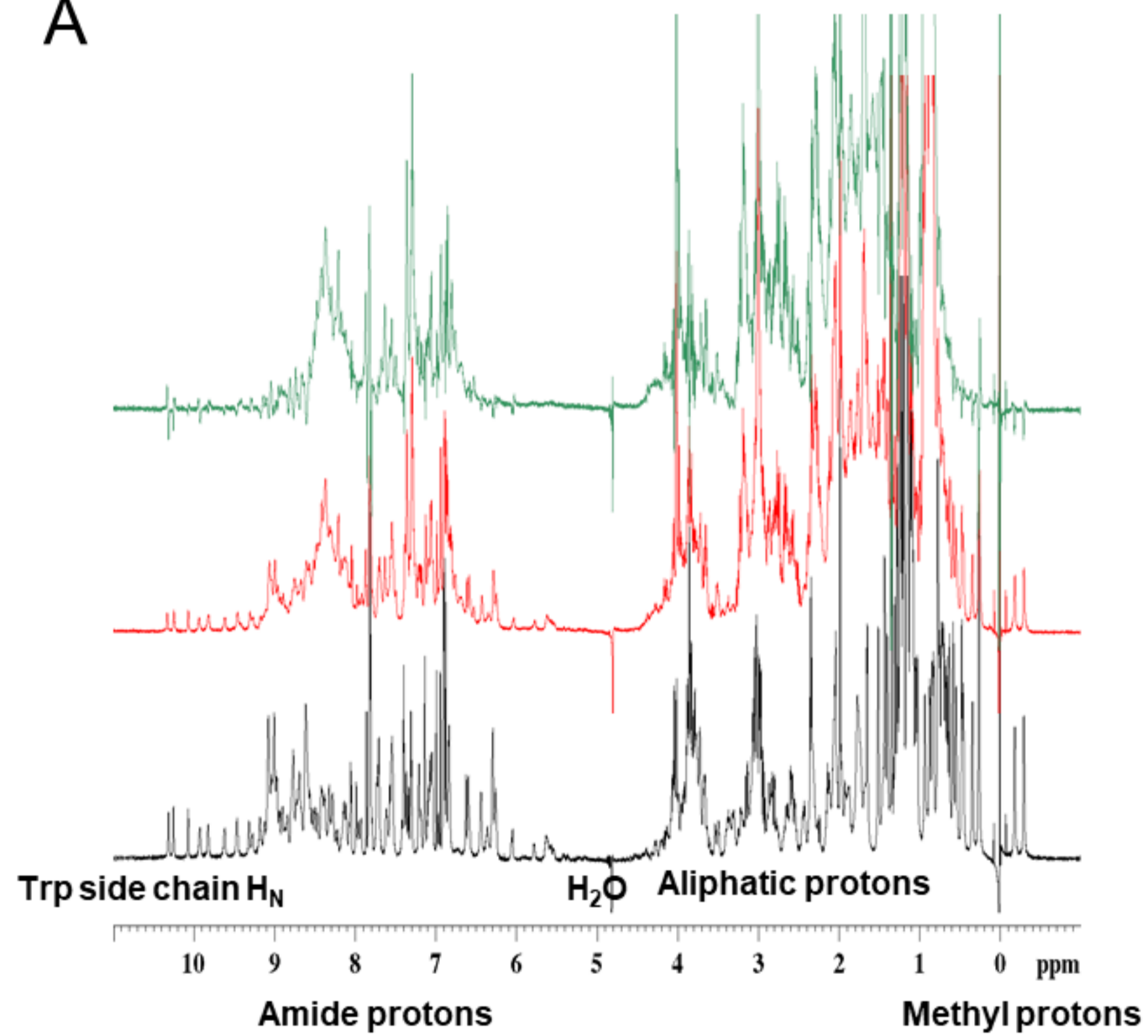
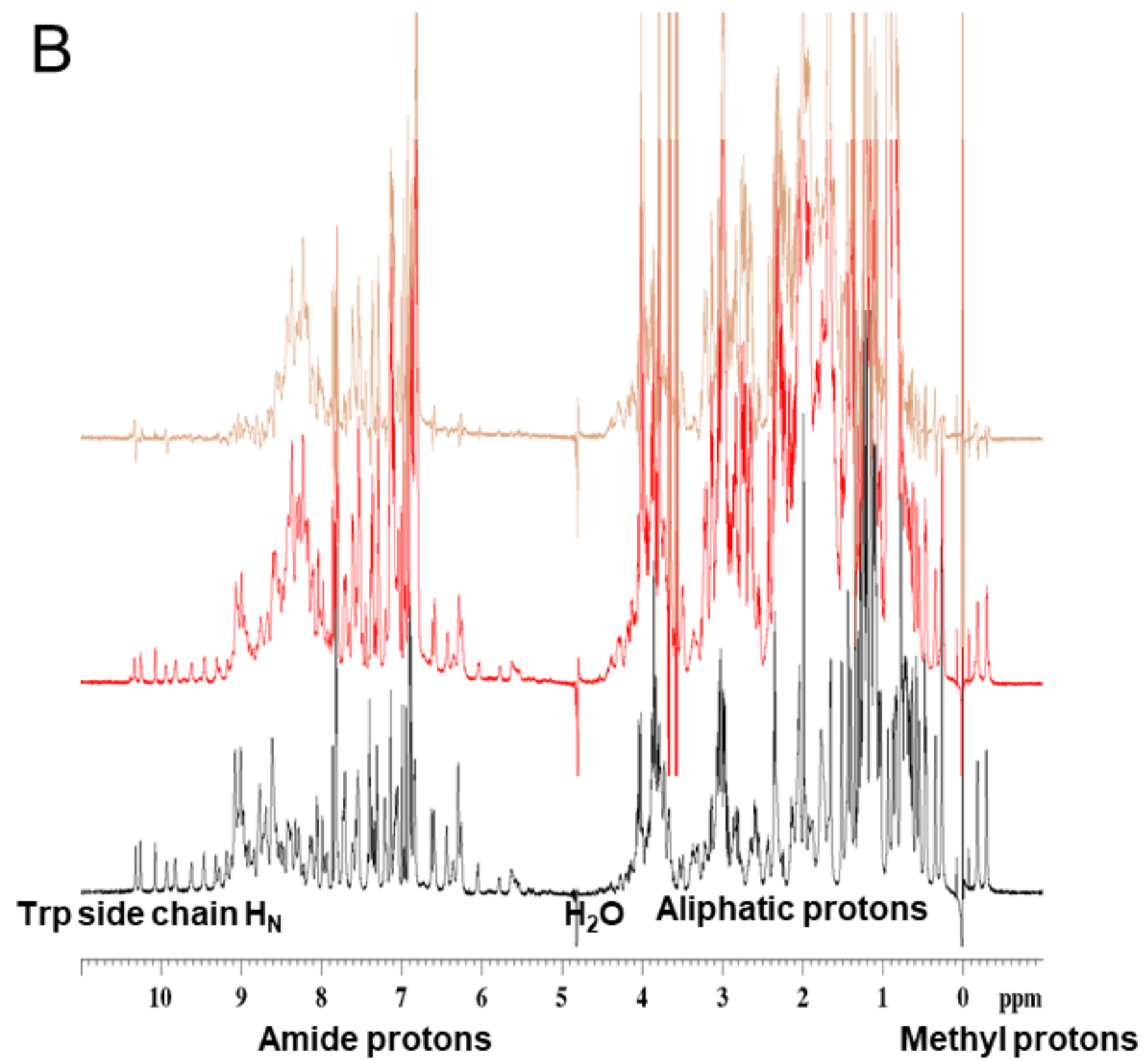
**A****B**

■ *NpXyn11A*   
 ✕ *NpXyn11A*-[In-Jo]-CBM2b-1   
 ● *NpXyn11A*-[Jo-In]-CBM3a   
 ✱ *NpXyn11A*-[Jo-In]-CBM2b-1   
 ▲ *NpXyn11A*-[In-Jo]-CBM3a   
 ◆ control

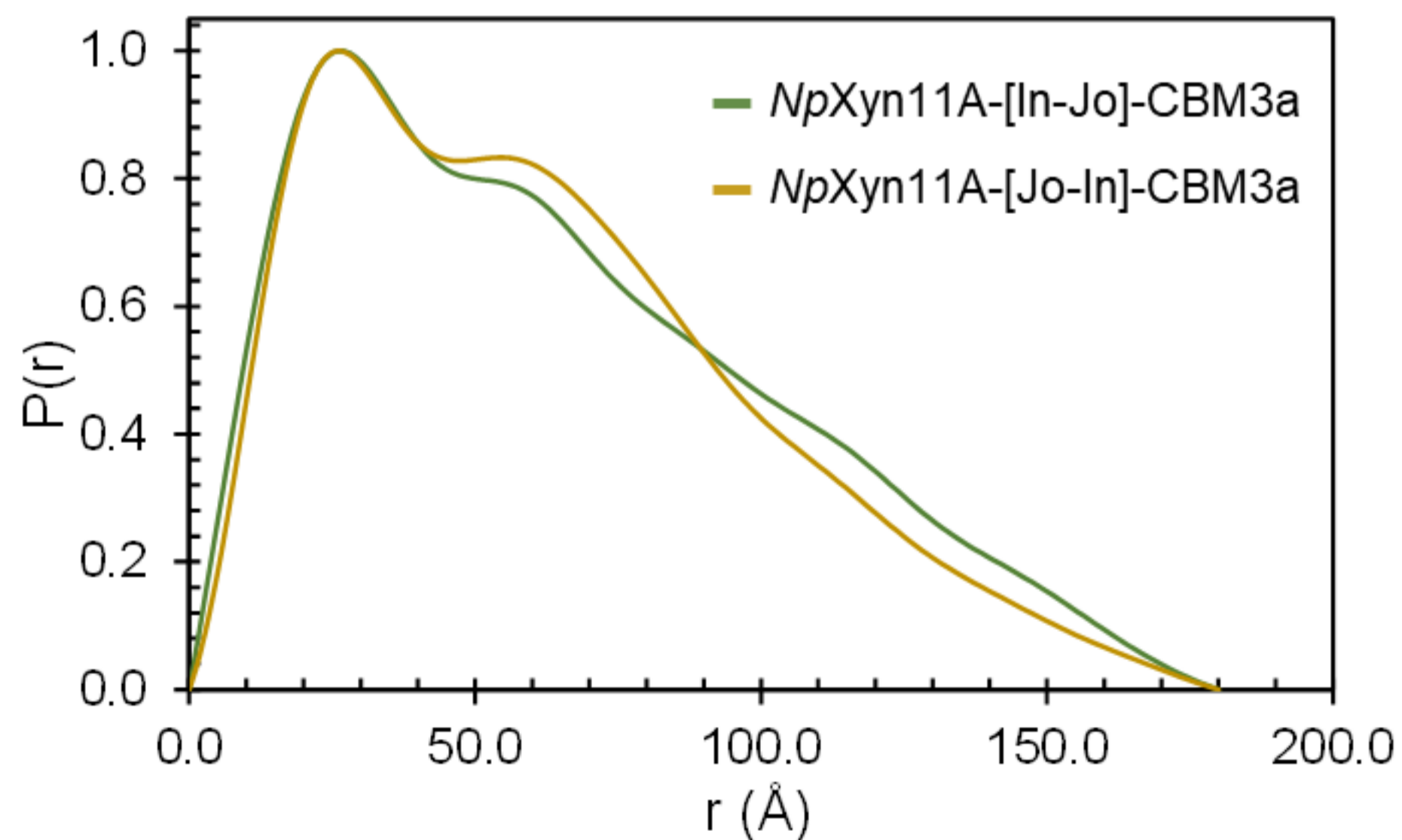
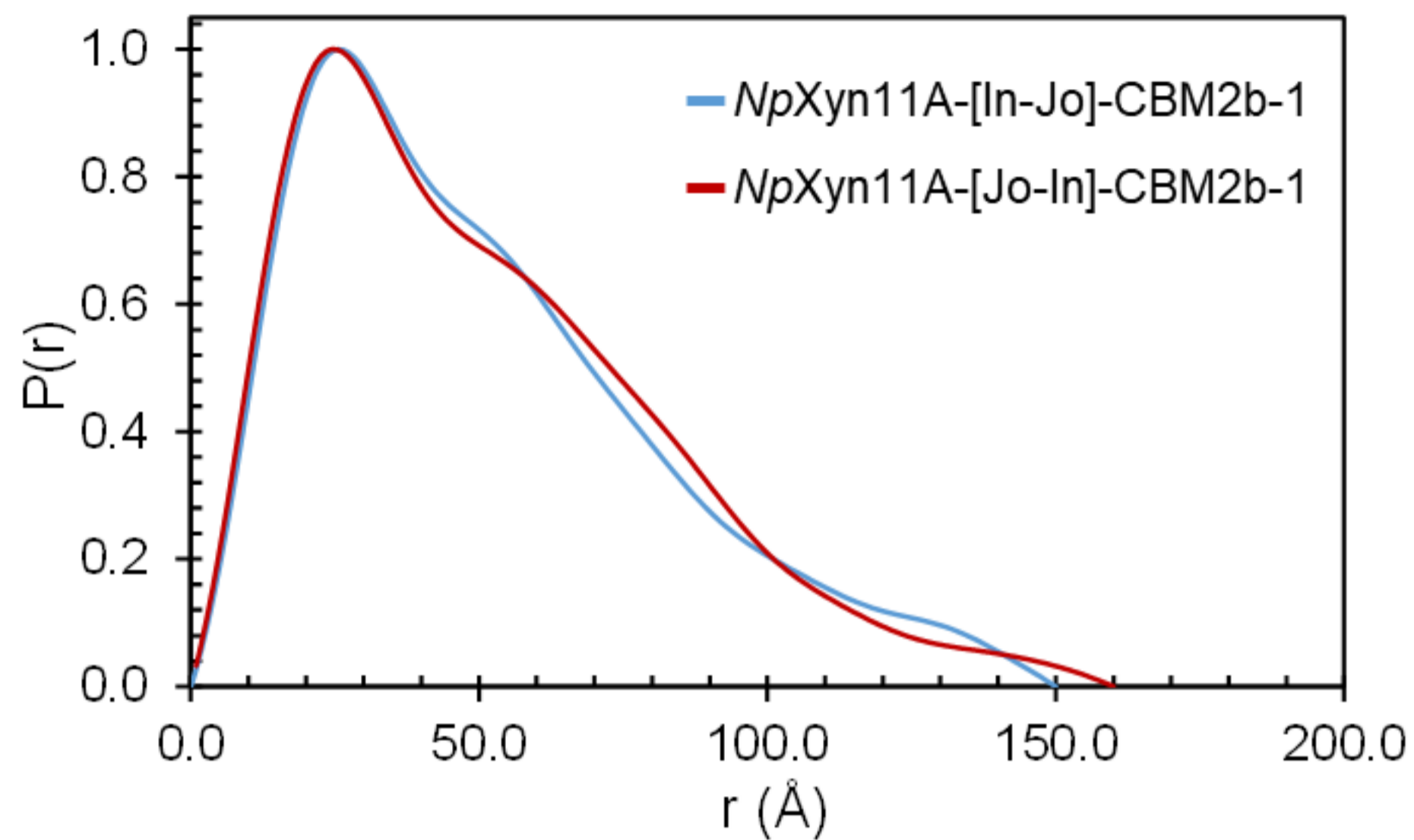
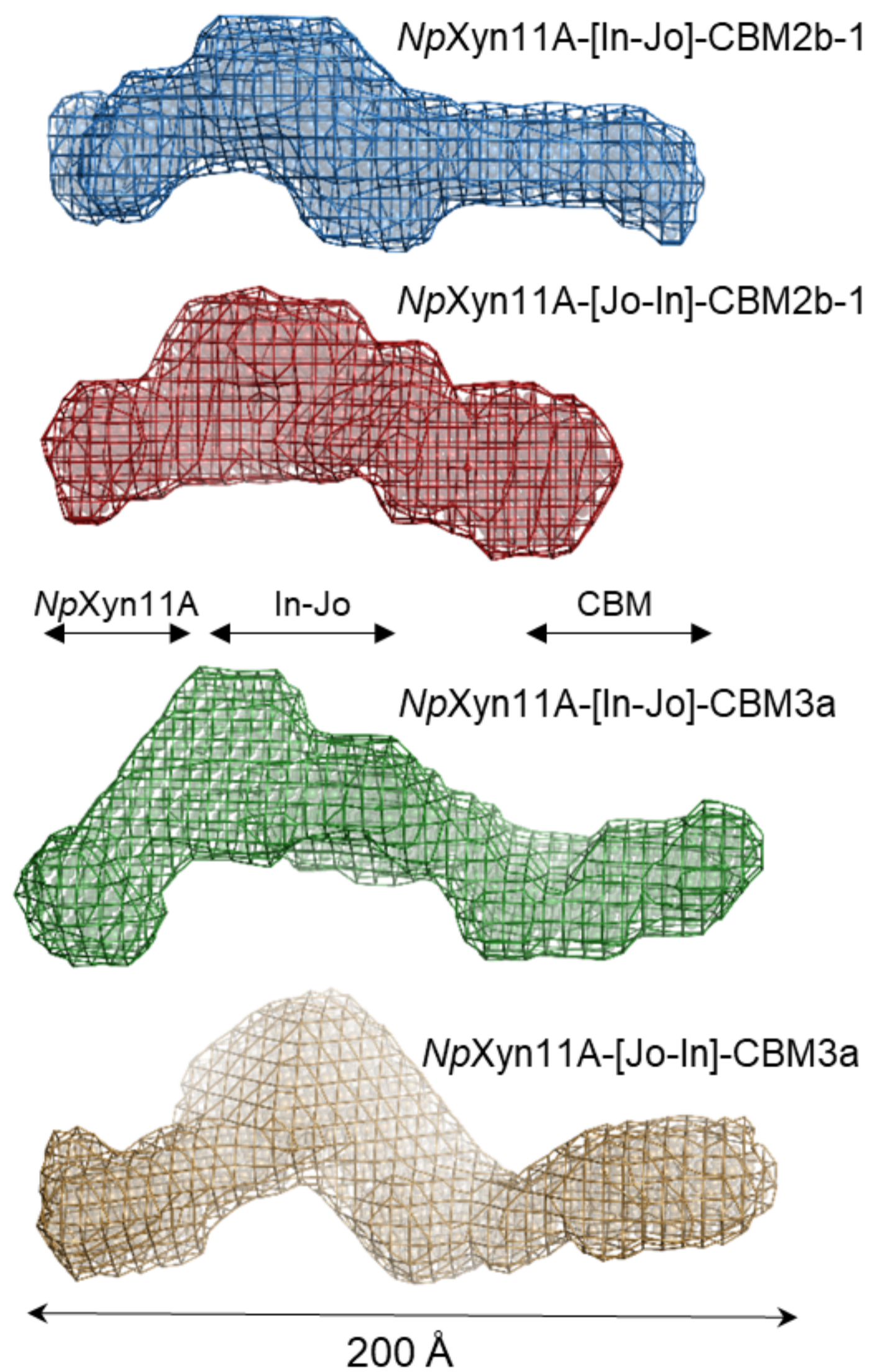


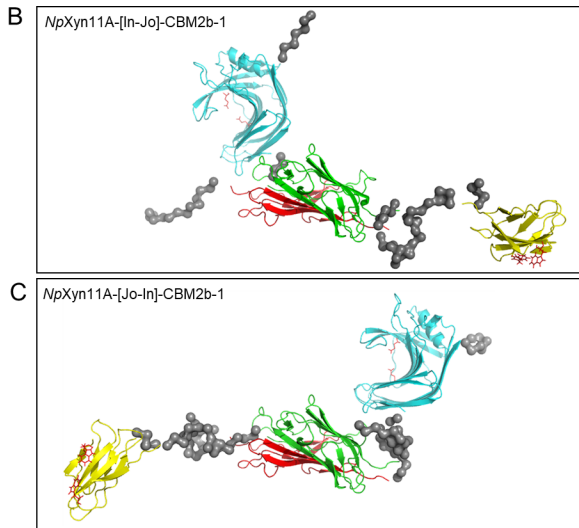
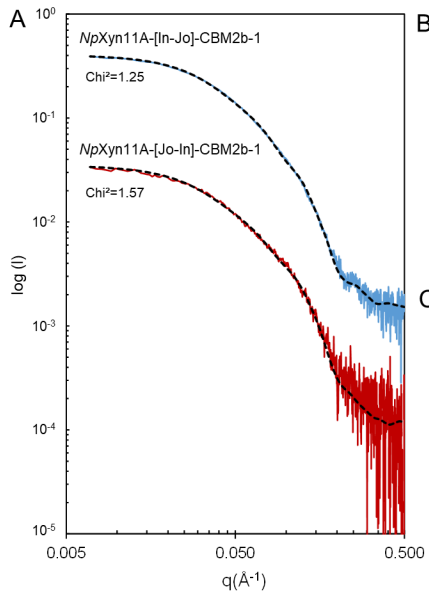
**C**

Sample	Molecular Mass (Kda)	Gyration radius $R_g$ (Å)	Maximal distance $D$ (Å)	Folding
<i>NpXyn11A</i> -[Jo-In]-CBM3a	71.7	47.8	185	Folded
<i>NpXyn11A</i> -[In-Jo]-CBM3a	71.0	46.5	180	Folded
<i>NpXyn11A</i> -[Jo-In]-CBM2b-1	63.4	42.1	160	Folded
<i>NpXyn11A</i> -[In-Jo]-CBM2b-1	62.7	41.8	150	Folded
Jo-CBM2b-1	21.1	46.1	190	Unfolded
In-CBM2b-1	27.0	58.0	210	Unfolded
In- <i>NpXyn11A</i>	41.5	46.2	160	Partially Folded
<i>NpXyn11A</i>	25.9	18.5	60	Folded

**A****B**



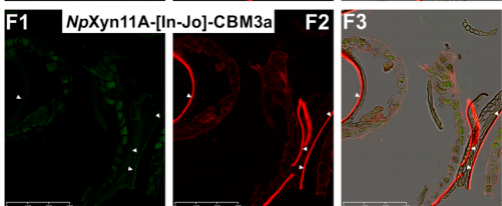
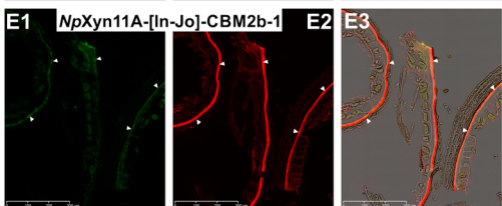
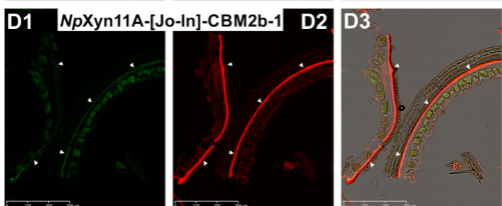
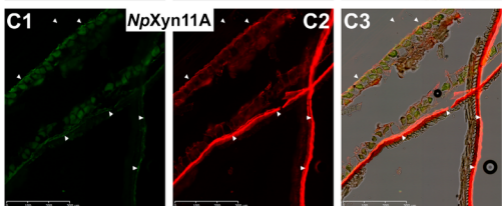
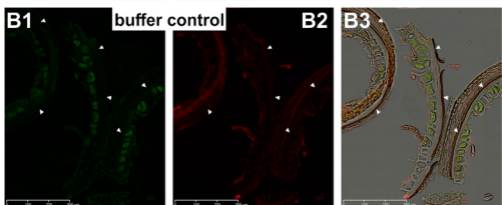
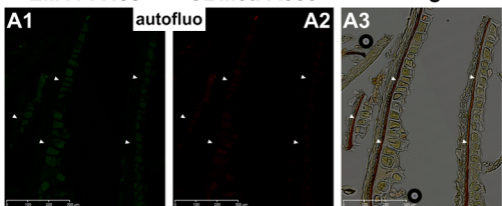
**A****B**



LM11-A488

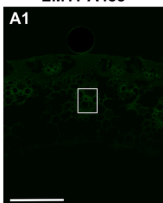
CBM3a-A555

Merge

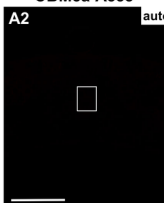




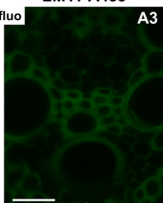
LM11-A488



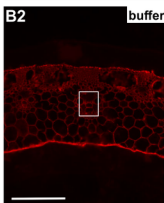
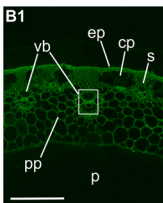
CBM3a-A555



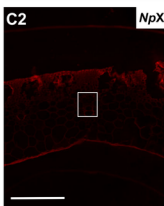
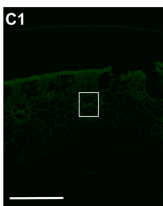
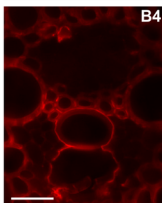
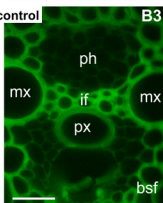
LM11-A488



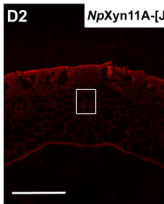
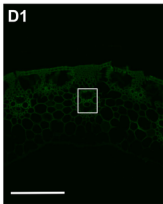
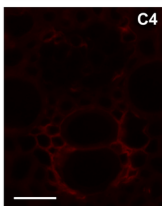
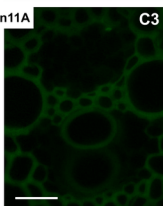
CBM3a-A555



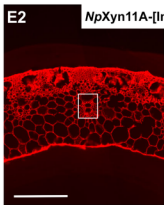
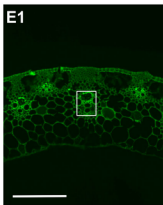
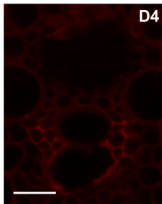
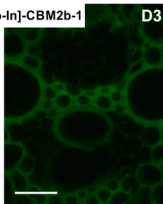
buffer control



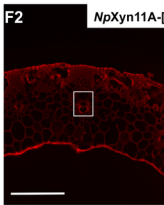
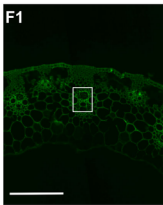
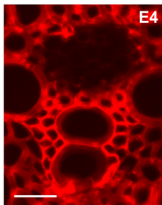
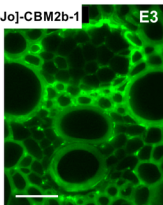
NpXyn11A



NpXyn11A-[Jo-In]-CBM2b-1



NpXyn11A-[In-Jo]-CBM2b-1



NpXyn11A-[In-Jo]-CBM3a

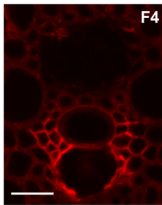
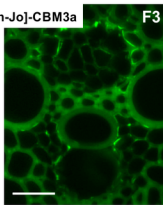


**Table 1:**

Protein	EC <sub>50</sub> (g·L <sup>-1</sup> )	
	<i>Buffer 1</i>	<i>Buffer 2</i>
In-CBM3a	-	0.003 ± 0.0001
CtCBM3a	0.14 ± 0.01	0.18 ± 0.04
Jo-CBM3a	0.21 ± 0.12	-

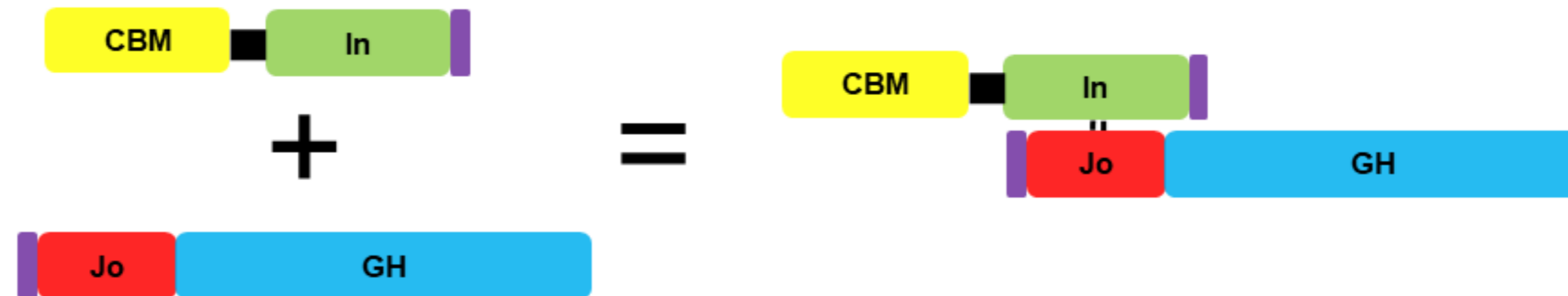
**Table 2:**

Protein	$K_d$ (mM)		
	This work (Trp 259)	This work (Trp 291)	[35]
<i>Cj</i> CBM2b-1	0.84	1.02	0.29
In-CBM2b-1	0.22	0.52	-
Jo-CBM2b-1	> 10	> 10	-

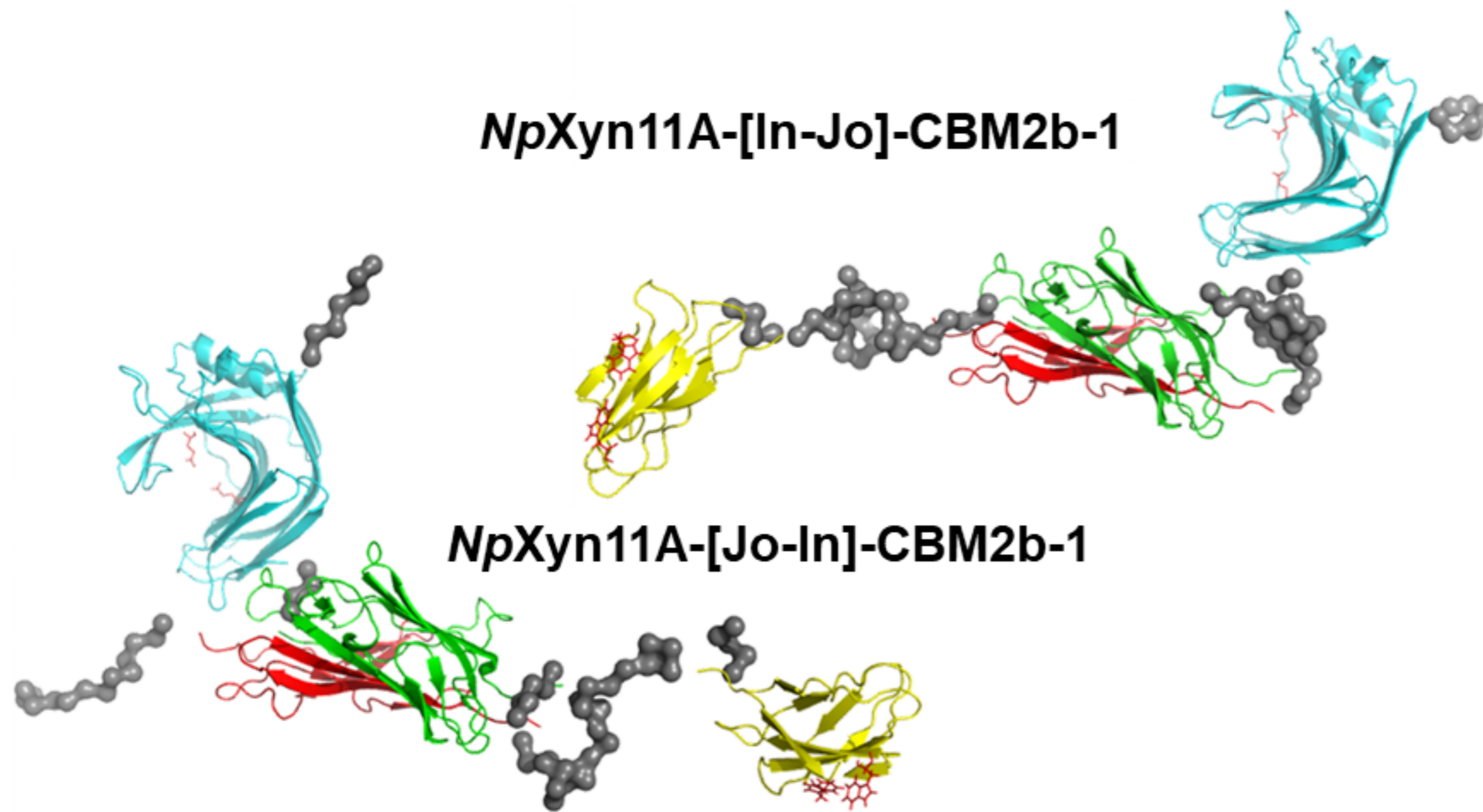
**Table 3:**

Single enzymes	Specific Activity			
	<b>pNP-X<sub>3</sub></b> (IU/ $\mu$ mole)	<b>WAX</b> 10 <sup>3</sup> (IU/ $\mu$ mole)	<b>RAX</b> 10 <sup>3</sup> (IU/ $\mu$ mole)	<b>BWX</b> 10 <sup>3</sup> (IU/ $\mu$ mole)
<i>NpXyn11A</i>	155.78 $\pm$ 4.07	114.59 $\pm$ 2.67	83.44 $\pm$ 8.21	65.03 $\pm$ 2.19
<i>In-NpXyn11A</i>	153.17 $\pm$ 1.68	-	-	-
<i>Jo-NpXyn11A</i>	124.63 $\pm$ 3.64	-	-	-
<i>NpXyn11A</i> -[In-Jo]-CBM3a	148.83 $\pm$ 14.19	87.29 $\pm$ 6.32	81.58 $\pm$ 3.03	53.30 $\pm$ 0.70
<i>NpXyn11A</i> -[Jo-In]-CBM3a	115.88 $\pm$ 25.78	160.72 $\pm$ 6.34	196.17 $\pm$ 0.60	93.40 $\pm$ 1.34
<i>NpXyn11A</i> -[In-Jo]-CBM2b-1	98.87 $\pm$ 4.01	62.81 $\pm$ 8.28	28.57 $\pm$ 3.03	39.50 $\pm$ 0.61
<i>NpXyn11A</i> -[Jo-In]-CBM2b-1	153.01 $\pm$ 5.30	126.91 $\pm$ 9.05	93.86 $\pm$ 9.59	58.30 $\pm$ 2.29

① Jo-In welding system = chimeric multi-modular enzyme



② Spatial orientation relatively locked



③ Optimal configuration in plant cell wall degradation

